



AFRL-OSR-VA-TR-2014-0075

---

**DEVELOPMENT AND APPLICATION OF ENERGETIC ACTUATORS FOR SHEAR AND VORTEX DOMINATE**

**Farrukh Alvi**  
**FLORIDA STATE UNIV TALLAHASSEE**

---

**03/06/2014**  
**Final Report**

**DISTRIBUTION A: Distribution approved for public release.**

**Air Force Research Laboratory**  
**AF Office Of Scientific Research (AFOSR)/ RTA**  
**Arlington, Virginia 22203**  
**Air Force Materiel Command**

<b>REPORT DOCUMENTATION PAGE</b>				<i>Form Approved</i> <b>OMB No. 0704-0188</b>	
<small>Public reporting burden for this collection of information is estimated to average 1 hour per response, including the time for reviewing instructions, searching existing data sources, gathering and maintaining the data needed, and completing and reviewing this collection of information. Send comments regarding this burden estimate or any other aspect of this collection of information, including suggestions for reducing this burden to Department of Defense, Washington Headquarters Services, Directorate for Information Operations and Reports (0704-0188), 1215 Jefferson Davis Highway, Suite 1204, Arlington, VA 22202-4302. Respondents should be aware that notwithstanding any other provision of law, no person shall be subject to any penalty for failing to comply with a collection of information if it does not display a currently valid OMB control number. <b>PLEASE DO NOT RETURN YOUR FORM TO THE ABOVE ADDRESS.</b></small>					
<b>1. REPORT DATE (DD-MM-YYYY)</b>		<b>2. REPORT TYPE</b>		<b>3. DATES COVERED (From - To)</b>	
<b>4. TITLE AND SUBTITLE</b>				<b>5a. CONTRACT NUMBER</b>	
				<b>5b. GRANT NUMBER</b>	
				<b>5c. PROGRAM ELEMENT NUMBER</b>	
<b>6. AUTHOR(S)</b>				<b>5d. PROJECT NUMBER</b>	
				<b>5e. TASK NUMBER</b>	
				<b>5f. WORK UNIT NUMBER</b>	
<b>7. PERFORMING ORGANIZATION NAME(S) AND ADDRESS(ES)</b>				<b>8. PERFORMING ORGANIZATION REPORT NUMBER</b>	
<b>9. SPONSORING / MONITORING AGENCY NAME(S) AND ADDRESS(ES)</b>				<b>10. SPONSOR/MONITOR'S ACRONYM(S)</b>	
				<b>11. SPONSOR/MONITOR'S REPORT NUMBER(S)</b>	
<b>12. DISTRIBUTION / AVAILABILITY STATEMENT</b>					
<b>13. SUPPLEMENTARY NOTES</b>					
<b>14. ABSTRACT</b>					
<b>15. SUBJECT TERMS</b>					
<b>16. SECURITY CLASSIFICATION OF:</b>			<b>17. LIMITATION OF ABSTRACT</b>	<b>18. NUMBER OF PAGES</b>	<b>19a. NAME OF RESPONSIBLE PERSON</b>
<b>a. REPORT</b>	<b>b. ABSTRACT</b>	<b>c. THIS PAGE</b>			<b>19b. TELEPHONE NUMBER (include area code)</b>

**DEVELOPMENT AND APPLICATION OF ENERGETIC ACTUATORS FOR  
SHEAR AND VORTEX DOMINATED FLOW CONTROL**

**AFOSR GRANT FA9550-09-1-0301**

**FINAL REPORT 2009-2013**



**F. S. Alvi** (Principal Investigator)  
Department of Mechanical Engineering  
Florida A&M University and Florida State University (FAMU-FSU)  
Florida Center for Advanced Aero-Propulsion (FCAAP)  
Tallahassee, FL 32310

## Executive Summary

Active supersonic flow control has been a significant challenge due to the high momentum and fast response times required to produce effective control. It was to this end that Johns Hopkins University/Applied Physics Laboratory (JHU/APL) developed the SparkJet Actuator (SJA) in collaboration with Florida State University under AFSOR sponsorship. This unsteady, fast-response actuator was characterized in detail under a range of quiescent conditions for an array of actuator designs, where each subsequent generation was improved based on prior results. The optimized actuator design was implemented and tested in supersonic flow conditions to characterize and understand the actuator and flow behavior in a canonical high speed flow.

The SparkJet actuator is a zero net mass flux device that generates synthetic jets through the use of an electrical discharge. Electrodes inside a cavity connected to a capacitor bank are discharged at prescribed frequencies. The high temperature from the electrical discharge increases the pressure inside the cavity, and an orifice array located on the cavity allows the air to escape, thus creating the jets used for flow control. In this collaborative research, JHU/APL was primarily responsible for the actuator design, modeling and characterization of the thermal processes within the actuator. The group at FSU focused on experimentally characterizing the properties of the unsteady *external* flow produced by the different variants of the SJA under quiescent and supersonic flow conditions in order to better understand the fundamental physical mechanisms.

A 1-D numerical model was developed by JHU/APL to predict actuator performance as function of cavity volume, energy deposition, number of orifices and orifice diameter, among others. Initial validation of actuator performance was experimentally carried out by JHU/APL through measurement of internal flow and thermal properties (within the actuator cavity). The actuators were delivered to FSU for more detailed studies focusing the unsteady flow properties produced by the SJA. The tests performed at FSU use a novel, laser-based microschlieren technique which was developed for this study. It provides images with very high spatial and temporal resolution thus leading to a detailed picture of the temporal evolution of the flow produced by the SJA. Such studies were

conducted for a number of SJA designs where the main parameters, such as orifice diameters, ambient pressures and electrode configuration were varied. The actuators have a very rapid response, where very high momentum jets can be produced in about 10  $\mu$ s. The high control authority and very short response time is one of the most noteworthy features of SJAs. One significant issue encountered which can make measurements very challenging is the significant amount of EMI produced by SJAs. Tests were also conducted with the SJA operating at frequencies up to 1 kHz, but only in short bursts due to limitations imposed by overheating of the actuator hardware. To further enhance performance an external flow source was added in one variation of the SJA. This version shows promising results in terms of overall effectiveness of the actuator.

The SJA was also tested in single shot as well burst mode with pulsing frequencies of 500 – 1000 Hz in the wall boundary layer of a supersonic wind tunnel at Mach 1.5. Time-resolved flow visualizations were used to examine the effect of the actuator on the external supersonic flow. With the present SJA design, the actuator flow dynamically generates an oblique shock with a maximum angle of 48°. Similar to quiescent flow conditions, the actuator response, and as a result its impact on the flow, is very rapid; changes in the external supersonic flow were measurable in less than 50  $\mu$ s. These results are promising for the future use of the device, both in terms of actuation frequency and control authority.

## Table of Contents

1. Introduction .....	9
1.1. Present Research – SparkJet Actuator.....	10
1.2. SparkJet Actuator – The Basics.....	10
1.3. SparkJet Actuator – Design Improvements .....	11
1.4. Resonance Enhanced Microjet Actuator (REM) .....	13
2. Experimental Details – Methods and Hardware.....	14
2.1. Laser-Based Microschlieren System (LBMS).....	14
2.1.1 LBMS Light Source .....	15
2.1.2 LBMS Conditioned Imaging .....	16
2.2. SparkJet Actuator - Designs and Operating Parameters .....	17
2.2.1 Reduced Ambient Pressure Testing .....	18
2.2.2 SparkJet Operating Modes .....	19
2.2.3 SJA Trigger Mechanism .....	20
2.2.4 SJA with Cavity Refill Supply .....	21
2.2.5 Wind Tunnel Tests – SJA and Model .....	22
3. Actuator Characterization under Quiescent Conditions .....	24
3.1. Single-Shot Operation of the SJA .....	24
3.1.1. Single Orifice SJA – Atmospheric Conditions .....	24
3.1.2. Four Orifice SJA – Atmospheric Conditions .....	28
3.1.3. Four Orifice Array Testing at Sub-Atmospheric Conditions .....	28
3.1.4. Effect of Trigger Mechanism on Flowfield Velocity .....	31
3.1.5. Four Orifice 400 $\mu\text{m}$ SJA with Pseudo-Series Trigger – Atmospheric Conditions with Various Active Refill Supply Pressures .....	32
3.1.6. Four Orifice 800 $\mu\text{m}$ SJA with Various Active Refill Supply Pressures .....	36
3.1.7. Effect of Orifice Diameter on Flowfield Velocity .....	37
3.2. Burst Mode Operation of the SJA .....	38
3.2.1. Burst Mode Discharge Reliability.....	39
3.2.2. 500 Hz Operation with Various Refill Supply Pressures (400 $\mu\text{m}$ Orifice).....	40
3.2.3. 700 Hz Operation with Various Refill Supply Pressures (400 $\mu\text{m}$ Orifice).....	42
3.2.4. 1 kHz Operation with Various Refill Supply Pressures (400 $\mu\text{m}$ Orifice).....	43
3.3. REM Actuator – Selected Results .....	44
4. SJA Performance in Supersonic Crossflow (Tunnel Experiments).....	47
4.1. Tunnel Facility and Test Conditions .....	47
4.1.1. Tunnel Flow Visualizations .....	48

4.2. Actuators under Quiescent Ambient Conditions .....	50
4.3. Baseline Results (No Actuation) .....	52
4.4. SJA in Single Shot Mode in Supersonic Crossflow .....	53
4.5. SJA in Burst Mode in Supersonic Crossflow .....	56
4.6. Comparison to Steady Microjets .....	58
4.7. REM Actuator – Selected Results .....	59
5. Summary and Conclusions .....	63
6. References .....	66
7. Supplemental Information .....	69
7.1. Publications (2008 – 2013).....	69
7.1.1. Archival Journal Publications Directly Related .....	69
7.1.2. Other Related Archival Journal Publications .....	70
7.1.3. Conference Proceedings .....	70
7.2. Students Supported under this Grant (Fully or Partially) .....	71
7.3. Honors and Awards (2009 – 2013) .....	72
7.4. Related Patents (2009 – 2013).....	72
Acknowledgement/Disclaimer .....	72

## List of Figures

1.1: SparkJet operation schematic .....	11
1.2: Comparison of SparkJet trigger mechanisms .....	12
1.3: SparkJet actuator with cavity refill supply .....	12
2.1: Schematic of the laser-based microschlieren system .....	15
2.2: A photograph of SJA used for some benchtop visualizations .....	16
2.3: Image Acquisition timing diagram for SJA visualizations.....	17
2.4: Four orifice actuator .....	18
2.5: Specially designed vacuum chamber with optical access .....	19
2.6: Operating efficiency with pseudo-series trigger mechanism .....	21
2.7: Actuator in wind tunnel .....	23
2.8: Bottom and rear views of the three-SJA assembly for wind tunnel tests .....	23
3.1: Time delayed schlieren images of the single 1 mm orifice SparkJet exhaust at atmospheric conditions .....	26
3.2: Blast wave and jet front propagation velocities at atmospheric conditions.....	27

3.3: 250 $\mu$ s and 550 $\mu$ s time delayed schlieren images at atmospheric conditions .....	27
3.4: Time delayed schlieren images of the SparkJet exhaust at atmospheric conditions .....	28
3.5: Time-resolved schlieren images of the four orifice SJA exhaust at 60 kPa .....	29
3.6: Blast wave and jet front velocity measurements .....	30
3.7: Blast wave and jet front velocity measurements .....	31
3.8: Time delayed schlieren images of the 400 $\mu$ m four orifice SparkJet exhaust with no refill supply .....	32
3.9: Time delayed schlieren images of the 400 $\mu$ m four orifice SparkJet exhaust with 1.4 psig refill .....	33
3.10: Time delayed schlieren images of the 400 $\mu$ m four orifice SparkJet exhaust with 3 psig refill .....	34
3.11: Time delayed schlieren images of the 400 $\mu$ m four orifice pseudo-series triggered SJA with various refill supply pressures.....	35
3.12: Blast wave and jet front velocity calculations of four 400 $\mu$ m orifice actuator with various refill supply pressures.....	36
3.13: Time delayed schlieren images of the 800 $\mu$ m four orifice pseudo-series triggered SJA with various refill supply pressures.....	37
3.14: Comparison of orifice diameter on jet front and blast wave velocities .....	38
3.15: Pressure measurements to examine the reliability of the SparkJet actuator during a 100 discharge firing sequence at 1 kHz.....	40
3.16: Qualitative data revealing the reliability of the SparkJet actuator during an 11 discharge firing sequence at 1 kHz.....	40
3.17: Burst mode operation of four 400 $\mu$ m SJA at 500 Hz with various cavity refill supply pressures.....	41
3.18: Burst mode operation of four 400 $\mu$ m SJA at 700 Hz with various cavity refill supply pressures.....	43
3.19: Burst mode operation of four 400 $\mu$ m SJA at 1 kHz with various cavity refill supply pressures.....	44
3.20: Phase conditioned microschlieren flow visualizations of a typical REM actuator flowfield .....	45
3.21: Unsteady acoustic spectra of the 1 kHz REM actuator designed for windtunnel testing .....	45
3.22: Qualitative comparison of density contours from simulation with experimental microschlieren images at representative phase angles .....	46
4.1: Layout of the supersonic wind tunnel .....	48
4.2: Phase-conditioned timing diagram for wind tunnel SJA tests.....	48
4.3: Wind tunnel testing hardware schematic.....	49
4.4: Shadowgraph images of the SJA array installed in the wind tunnel operating in single-shot mode with no freestream flow .....	51



4.5: Instantaneous shadowgraph images of the SparkJet array installed in the wind tunnel operating in burst mode with no freestream flow in the test section.....	51
4.6: Baseline, no actuator flow, shadowgraph image of the test section .....	52
4.7: Phase-conditioned shadowgraph images of the SJA array (single-shot mode) in Mach 1.5 flow at various time delays.....	54
4.8: Oblique shock angle evolution .....	55
4.9: Phase-conditioned shadowgraph images showing boundary layer interaction in Mach 1.5 flow .....	56
4.10: Phase-conditioned shadowgraph images of SJA operating at 700 Hz in burst mode .....	57
4.11: Oblique shock angle evolution comparing first and last discharge of the actuator operating in burst mode at 700 Hz .....	58
4.12: Oblique shock angle resulting from steady microjet injection and from the SparkJet actuator .....	59
4.13: Phase-conditioned images of a ~1 kHz REM actuator inside the supersonic tunnel without flow .....	60
4.14: Shadowgraph images of REM actuation into Mach 1.5 crossflow. ....	61
4.15: Angle of the actuator-generated oblique shock throughout the actuator cycle. ....	61
4.16: Comparison of REM actuator performance to steady microjet injection. ....	62

## 1. Introduction

Various classes of flow control actuators have provided varying degrees of benefit in terms of aerodynamic and/or acoustic performance by influencing the boundary layer or the shear layer of the flowfield. In principal, natural flow characteristics such as transition, turbulence, flow separation, mixing etc. can potentially be controlled: suppressed, attenuated or enhanced, more efficiently through active flow control (AFC) schemes that use appropriate actuation methods.

As an example, flow separation over an airfoil is an important practical problem where unsteady actuation techniques have been extensively studied for its control. Seifert et al. (1996) have shown that periodic excitation by momentum addition, with a frequency higher than the natural vortex shedding frequency, may achieve similar gains in performance in comparison with steady blowing, with 99% less momentum. McManus and Magill (1996) used pulsed angular injection to create co-rotating vortices to attach separated flow. This actuation technique reportedly worked well for high angles of attack and is referred to as pulsed vortex generators. Bryant et al. (1999), Wiltse and Glezer (1993) and Smith and Glezer (1998) used piezoelectric actuators for imparting unsteady momentum for flow separation control. These actuators, also called synthetic jets, produce zero net mass flux (ZNMF) jets with velocities in the range of 10-80 m/sec at a frequency range up to 1 kHz. This technology has been developed further with input from many others on the modeling, design and fabrication of compact ZNMF actuator systems (Cattafesta et al. (2000) and Joslin et al. (1999)).

Although some of the above actuators produced promising results for various subsonic applications, they are ineffective when flow velocities are high. Hence, devices and techniques applicable to high-speed flows, especially for supersonic and hypersonic flows, are still limited and continue to be an active area of research. As an example, the highly unsteady flowfield of an impinging supersonic jet or the flowfield inside a cavity, such as a weapon/cargo bay of a fighter aircraft subjected to cruise conditions from high subsonic to supersonic speeds, are examples of flows that demand unsteady, high-amplitude actuation techniques. Such high-speed flows require actuators that can provide

high mean and unsteady momentum. Moreover, in most applications, the unsteady properties of the base flows largely depend on operating conditions that vary over a wide range of frequencies. An actuator with high unsteady momentum whose frequency can be tuned over a large bandwidth will be useful for such applications. Some of the AFC devices tested for high-speed flow control include steady blowing using high-momentum microjets. Steady microjets have successfully demonstrated their efficacy as AFC actuators, where effects range from the reduction of unsteadiness in supersonic cavities (Zhuang et al. 2006) to noise reduction and lift enhancement in impinging jet flowfields (Alvi et al. 2008). Although the effect of steady control has been significant in most applications, research has also demonstrated that pulsing the jets (unsteady operation) may produce further benefits (Ali et al. 2010). Resonance Enhanced Microjet (REM) actuators capable of unsteady actuation, production of high-amplitude oscillations, and operation over a large bandwidth with slight modification to the geometry or pressure have been characterized in Mach 1.5 flow over a cavity (Ali et al. 2010) and also over a flat plate (Topolski et al. 2012).

More recently, research has focused on developing plasma actuators for AFC. Some noteworthy features of plasma actuators which make them attractive for AFC include: no mechanical/moving parts, very low or zero mass flow requirements, high bandwidth actuation, fast response times, and precise phase control. Plasma actuators are of several different types, namely surface discharge plasmas, MagnetoHydroDynamic (MHD) plasmas, Localized Arc Filament Plasma Actuators (LAFPA), and SparkJets. The interaction of surface discharge plasma actuators with the boundary layer on a flat plate in a Mach 5 flowfield has been studied by Shang et al. (2008). Magnetically driven surface plasma actuators (Kalra et al. 2007 and Kalra et al. 2009) have been used for flow control in a shock wave induced boundary layer separation in Mach 2.6 and 2.8 flowfields. LAFPA are unsteady actuators with a very wide bandwidth and high amplitude capable of affecting a large range of jet Mach numbers (Samimy et al. 2004) and also the interaction of a turbulent boundary layer with an oblique shock wave in a Mach 1.9 and 2.33 flowfield (Samimy et al. 2007 and Caraballo et al. 2009). Pulsed-

plasma jets (Webb et al. 2013) have been developed for high-speed flow control and tested in a Mach 3 flowfield.

### **1.1. Present Research – SparkJet Actuator**

For flow control to be widely applicable and practical, actuators should ideally be capable of performing at frequencies that are naturally present in the base flowfield. For a vast range of high-speed flow regimes and applications, this translates to a need for actuation ranging from several hundred hertz to a few kilohertz, or even higher. The actuators must also be capable of producing high-amplitude mean as well as unsteady perturbations over a large dynamic range. Many existing unsteady actuators do not meet these requirements of producing both a high-amplitude mean and fluctuating components with frequency modulation. Under the Air Force Office of Scientific Research (AFOSR) sponsorship, Florida State University's Florida Center for Advanced Aero-Propulsion (FSU-FCAAP), in collaboration with The Johns Hopkins University Applied Physics Laboratory (JHU/APL), have been investigating the SparkJet Actuator (SJA) that holds the promise of manipulating high-speed flows without moving parts or aerodynamic structures. In this report we summarize the results of the study conducted at the Florida State University that focuses on experimentally characterizing the properties of the unsteady flow produced by the SparkJet. Emphasis is placed on the experimental results obtained on 'benchtop experiments' acquired under quiescent conditions and the implementation of the SJA in supersonic flow. The details of the SparkJet actuator design and modeling results are described in a companion report compiled by our collaborators at the JHU/APL. Next, we provide a very brief overview of the SJA.

### **1.2. SparkJet Actuator – The Basics**

The basic SparkJet actuators consist of a cavity, electrodes, and a single or multiple orifice(s). Advantages of this type of actuator include the lack of mechanical/moving parts, a net mass flow reduction, a fast response time, and the ability to control the discharge frequency and momentum throughput. The actuators have the same method of operation as the single SparkJet devices used in previous studies by the group at JHU/APL (Cybyk et al. 2005, Cybyk et al. 2006 and Haack et al. 2011) and

schematically described in Figure 1.1. The operation cycle consists of three distinct stages: energy deposition, discharge, and recovery. High cavity pressure is generated by rapidly heating the air inside of the SparkJet cavity by means of an electrical discharge. The pressurized air then discharges through the array orifice(s) creating high-speed jets intended for control authority. Following the discharge, the cavity is refilled, and the cycle is repeated.

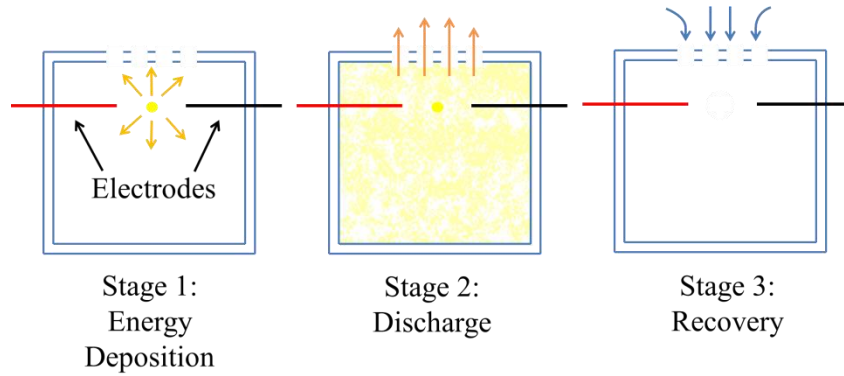


**Figure 1.1:** SparkJet operation schematic.

The input energy ratio of the SparkJet actuator,  $Q/E$  (Equation 1.1), is defined as the ratio of the energy deposited by the SparkJet electrical discharge ( $Q$ ) to the internal energy ( $E$ ) of the air inside of the SparkJet cavity prior to heating.  $C$  is the capacitance across the sustain electrodes,  $V$  is the voltage across the sustain electrodes,  $m$  is the mass of air inside of the cavity,  $C_v$  is the heat capacity of the air inside of the cavity, and  $T$  is the temperature of the air inside of the cavity. For further details, please see final report from JHU/APL.

$$\frac{Q}{E} = \frac{0.5CV^2}{mC_vT} \quad (1.1)$$

### 1.3. SparkJet Actuator – Design Improvements

Throughout the course of this research, the SJA has gone through several design modifications with the aim of improving its reliability, control authority and dynamic range. Representative results from the earlier versions (Cybyk et al. 2005 and Cybyk et al. 2006) as well as the subsequent improved versions are discussed in this report. Very

briefly, the early generation SJA designs clearly demonstrated its ability to produce a jet with high exhaust velocities capable of manipulating high-speed flows. Computational and experimental studies of the first generation design (Cybyk et al. 2006) have led to design modification in terms of the electrode configuration, cavity volume, and orifice size leading to substantial improvements in the SparkJet range and efficiency, where for example, the efficiency has been increased from 20-30% to 70% at atmospheric pressure. (Haack et al. 2011)

The efficiency enhancement in later generations of SJAs is partly due to the improvements in the electrical discharge trigger mechanism. The original SparkJet design incorporates two sustain electrodes and a third trigger electrode as seen in Figure 1.2a whereas a subsequent design uses a trigger mechanism incorporated into the two sustain electrodes, referred to as the *pseudo-series trigger mechanism*; this is seen in Figure 1.2b. Results from different generations of SJA are discussed in chapter 3 of this report. Additional changes made to the actuator include the incorporation of a cavity refill air supply. As subsequent results demonstrate, the refill supply air reduces the refresh time and may aid in high frequency testing; this version of the SJA can be seen in Figure 1.3.

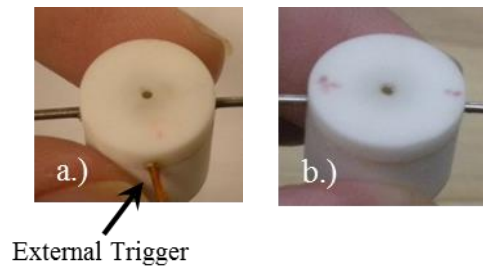


**Figure 1.1:** Comparison of SparkJet trigger mechanisms; a) External trigger design using three electrodes; b) Pseudo-series trigger using two electrodes.

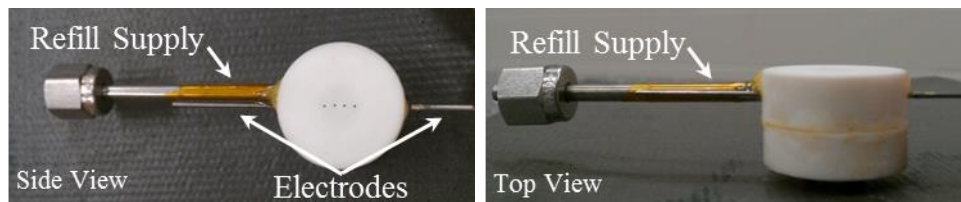


**Figure 1.2:** SparkJet actuator with cavity refill supply.

#### **1.4. Resonance Enhanced Microjet Actuator (REM)**

In addition to the SparkJet studies, a small part of the resources under this grant were also utilized to develop and examine the flowfield of a novel, high-bandwidth micro fluidic actuator developed at FSU. This compact micro fluidic actuator system, referred to as a Resonance Enhanced Microjet actuator (REM) consists of an underexpanded primary source jet impinging upon a cavity from which an array of *unsteady supersonic microjets emanate*. This design takes advantage of multiple flow-acoustic coupling phenomenon which allow for excellent control of the actuator frequency over a wide range through a number of actuator design parameters. Our studies have demonstrated that through an appropriate combination of geometric and fluid parameters, the actuator frequency can be tuned to any value roughly between 100 Hz - 70+ kHz. Detailed results on the REM actuators have been reported in Solomon (2010) and Solomon et al. (2010, 2013).

## **2. Experimental Details – Methods and Hardware**

In this section we present some details regarding the various actuator designs examined in the present study and discuss the diagnostics (some of it highly specialized) used for benchtop and wind tunnel studies. As the results discussed subsequently illustrate, the experimental characterization leans heavily on optical methods in large part due to the ElectroMagnetic Interference (EMI) issues encountered with SJA (also a challenge with most plasma-based actuators) as well as the very short time and length scales associated with the SJA flow which often make conventional sensor-based diagnostics difficult and less reliable.

### **2.1. Laser-Based Microschlieren System (LBMS)**

The very small physical scales associated with this flow required the use of a high-magnification microschlieren system. The small scales combined with the high speeds associated with the actuator flowfields under investigation required the exposure times for the images to be very short if the flow is to be ‘frozen’ in instantaneous realizations. After experimenting with various light sources, including high frequency pulsed LEDs, a laser based light source was found to be most appropriate. All of the images presented here from the benchtop studies were acquired using the Laser-Based Microschlieren System (LBMS) schematically shown in Figure 2.1. Excluding the light source, the microschlieren system is similar to that developed by Phalnikar et al. (2007). Initially, the light passes through a rectangular slit, which is used to create sharp edges on the light source. Although different arrangements can and were used depending upon the requisite field of view, a typical LBMS arrangement used plano-convex 25.4 mm diameter  $f/2.4$  lenses for acquiring zoomed-in images of the actuator flowfield. A knife edge was selected for the schlieren cut-off to increase the sensitivity of the system, where previously Scroggs and Settles (1996) and Phalnikar et al. (2007) used a graded cut-off in order to reduce the effects of diffraction. A 28-200 mm variable focal length camera lens was normally used to provide a magnified field of view. Kodak Megaplug and LaVision cameras were used to acquire the images using proVISION<sup>TM</sup> and DaVis software.



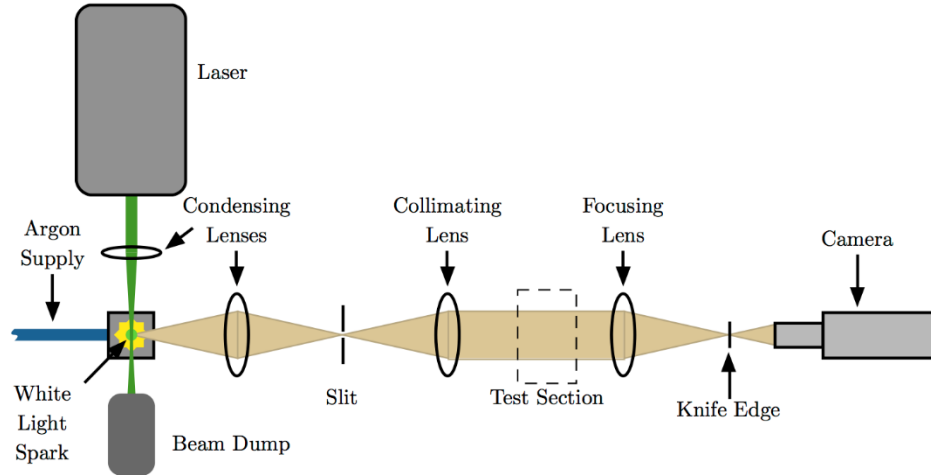


**Figure 2.1:** Schematic of the laser-based microschlieren system.

### 2.1.1. LBMS Light Source

The broadband white light for the schlieren system is generated from laser-induced breakdown in argon. A New Wave Gemini PIV laser was selected due to its short pulse duration of 3-5 ns, which was found by Volpe and Settles (2006) to sustain the plasma for 10 ns. The laser is focused using a 25.4 mm, f/1.0 plano-convex lens, selected due to the size and placement of other necessary optics. A tank of compressed argon was regulated to supply approximately 4 L/min onto the spark, where higher flow rates showed no effect on the plasma. The use argon in the cell was found to increase the light intensity of the spark 3-4 times compared to breakdown in air, and to decrease the jitter of the spark in the beam direction of the laser (Volpe and Settles 2006). The argon cell is made from a square tube of aluminum with an aluminum cap on each end. Both caps have a ~50 mm diameter cut out for the laser to pass through the cell. There is also a ~50 mm diameter hole on the side of the cell for passage of the white light generated by the breakdown. This white light is captured by a camera lens as shown in Figure 2.1. On the top of the argon cell are 1/4" NPT threads to easily attach the argon feed line connected to the high pressure storage tank. The inside of the cell is covered with adhesive backed black felt, which helps eliminate reflections inside the chamber. Further details on LBMS can be found in Foster (2011) and Foster et al. (2011).

Although the argon assisted in reduction of the jitter, it was still present, and the knife edge had to be used parallel to the laser beam direction. The light from the breakdown is focused onto the rectangular slit of the microschlieren system using a 50 mm, f/1.4 camera lens. The height of the slit was minimized in order to further increase the sensitivity based on Equation 2.1 from Settles (2006).  $S$  is the schlieren sensitivity;  $f_2$  is the focal length of the second schlieren lens; and  $a$  is the unobstructed height of the light source image in the cutoff plane. In this case,  $f_2$  is fixed in order to achieve the required magnification.

$$S = \frac{f_2}{a} \quad (2.1)$$

### 2.1.2. LBMS Conditioned Imaging

A photograph of an early generation of SJA used in benchtop characterization is shown in Figure 2.2. As seen here, in this model both sides walls of the cavity are made of optical quality glass allowing optical access. Also seen here are the three electrodes protruding through the Macor piece which supports the electrodes.

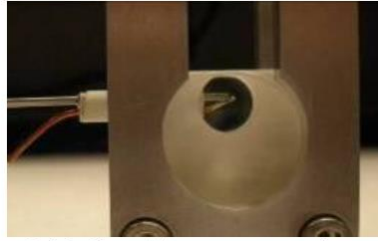


**Figure 2.2:** A photograph of SJA used for some benchtop visualizations.

In order to obtain time-resolved images accurately, the SJA was arranged such that a Scientech 301-020 photodiode could be placed against one of the optical windows to record the timing of the electrical discharge by measuring the light output from the plasma created. The photodiode signal and the Q-switch signal from the laser were recorded using an NI PCI card. Although the SJA fires consistently, there is a small amount of jitter, around  $\pm 1\mu s$ , between the signal sent to fire the SparkJet and the electrical discharge. In most cases, the photodiode and Q-switch signals were compared to accurately determine the timing of each image captured.

A representative diagram of the setup used for acquiring the images of the SparkJet actuator is shown in Figure 2.3. The camera software was used to trigger both the camera and the laser. A delay generator was used to trigger the SparkJet by increasing the delay between the SparkJet signal and the camera signal. Images were taken of the SparkJet actuator at multiple delay times by adjusting the signal from the delay generator to the SparkJet relative to the Q-switch. The SJA is triggered off of the flash lamp signal and delayed based on the delay between the flash lamp and the Q-switch. The trigger signals can be seen in Figure 2.3. Images acquired at different delays using the laser-based microsclieren system were used to measure jet front and blast wave velocities of the SparkJet exhaust. Note that the actual delay times used varied somewhat, based on the particular actuator design. A similar arrangement was used for REM visualizations as well, the main difference being that a microphone sensor was used to determine the actuator frequency and serve as a reference for phase-conditioned image acquisition. Details can be found in Foster et al. (2011) and Solomon et al. (2010, 2013).

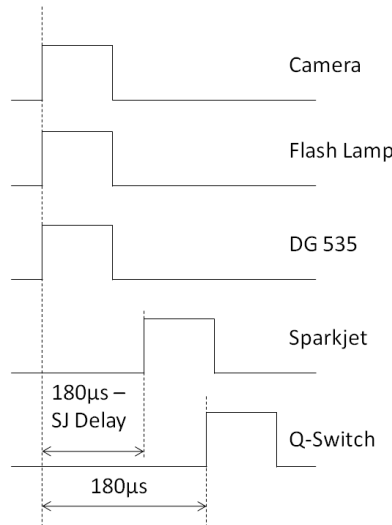


**Figure 2.3:** Image Acquisition timing diagram for SJA visualizations.

## 2.2. SparkJet Actuator – Designs and Operating Parameters

The process of developing, studying, and improving the SparkJet actuator has led to a variety of SparkJet actuators being characterized under different test conditions, as follows. The first SparkJet presented in this study consists of a 356 mm<sup>3</sup> cavity, *two*

*sustain electrodes* spaced 1.5 mm apart, *one external trigger electrode*, and a single 1 mm diameter orifice. Similar actuators having four 400  $\mu\text{m}$  diameter orifices spaced 1.5-2 mm apart were also examined and are shown in Figure 2.4. The multi-orifice actuator represents one third of the array that was tested in the wind tunnel (discussed in §2.2.5). The total capacitance across the sustain electrodes of these actuators was 13  $\mu\text{F}$  charged to 600 V resulting in an energy ratio ( $Q/E$ ) of 25. The trigger electrode is supplied with a voltage of 1-12 kV. The flow created by an actuator employing an external trigger mechanism is then compared to the flowfield generated by a different actuator, one that employs a *pseudo-series trigger mechanism* as first noted in §1.3. Actuators that employ a pseudo-series trigger have a capacitance of 7  $\mu\text{F}$  charged to 600 V across the electrodes (spaced 3 mm apart) resulting in an energy ratio ( $Q/E$ ) of 13. Further details on the pros and cons of the different electrode configurations can be found in Emerick (2013). The effect of orifice diameter on SparkJet performance is also examined. The effects of several cavity refill air supply pressures on the flow dynamics of the actuator are compared while the actuator operates in single shot and burst modes.

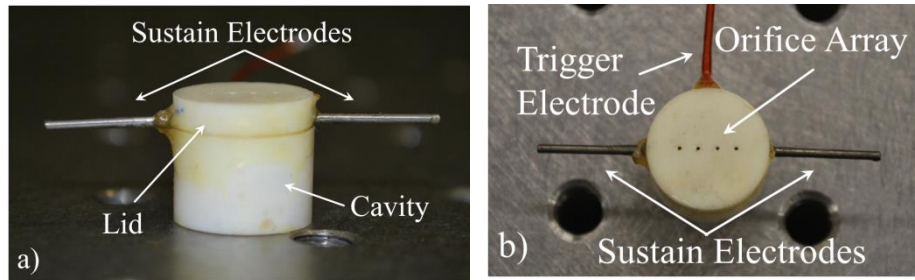


**Figure 2.4:** Four orifice actuator; a) side-view, b) top-view.

### 2.2.1. Reduced Ambient Pressure Testing

The actuator with four 400  $\mu\text{m}$  diameter orifices was characterized at ambient atmospheric conditions and at an absolute pressure of 60 kPa. The reduced ambient pressure conditions were meant to roughly simulate the ambient pressure boundary experienced in the supersonic wind tunnel. In benchtop studies, these conditions were established through the use of a custom built vacuum chamber as shown in Figure 2.5. The vacuum chamber allows for optical access on two sides and incorporates three electrical feed-through ports to accommodate two sustain electrodes, a trigger electrode,

and a pressure sensor. Following the completion of benchtop tests, some modifications were made to the wind tunnel causing the tunnel operational static pressure to be  $\sim 35$  kPa. Although there is a discrepancy between the benchtop and tunnel static pressures, the sub-atmospheric benchtop tests clearly reveal the effect of reduced pressures on SparkJet performance.

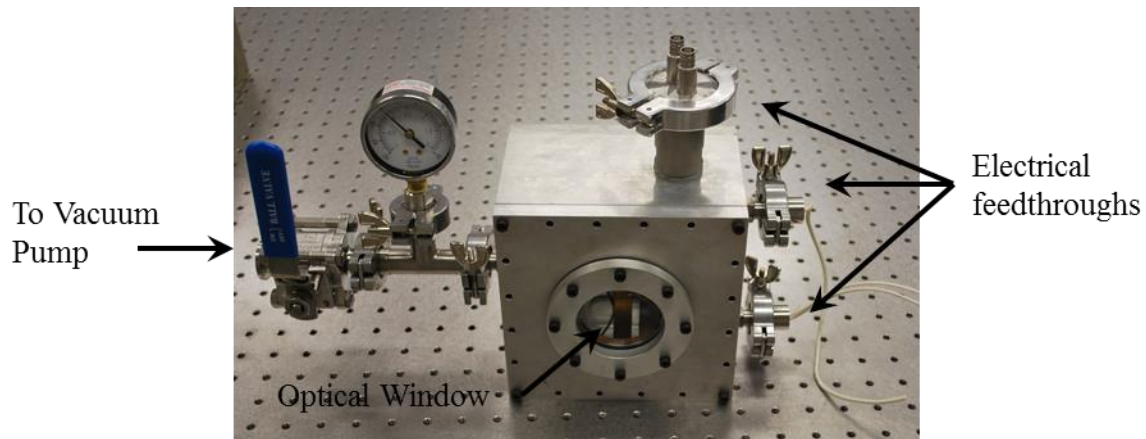


**Figure 2.5:** Specially designed vacuum chamber with optical access.

### 2.2.2. SparkJet Operating Modes

The SparkJet actuator has two modes of operation: single-shot mode and burst mode. In single-shot mode, the SparkJet is operated through a single discharge at a frequency of 1 Hz or lower. In burst mode, the SparkJet array is operated at frequencies up to 1 kHz for a fixed number of discharges. Control of burst mode is achieved using an Agilent 33521A Function/Arbitrary Waveform Generator. The burst mode is used for a large number of studies to prevent overheating of the electrodes and the air, a problem that occurs in continuous discharge operation. When this occurs, the sustained elevated temperature in the SJA components can cause “thermal runaway” where the actuator continuously discharges and becomes uncontrollable. As the results will show, in the benchtop studies, this burst mode has been successfully implemented at 1 kHz for up to 1 second without encountering thermal runaway.

### 2.2.3. SJA Trigger Mechanism

The electrical discharge of the SparkJet actuator is initiated by a short duration, high voltage spark that ionizes the air around the two sustain electrodes. This leads to an intense electrical discharge between the electrodes, followed by the rapid heating of the air inside of the cavity, and culminating in the high pressure discharge through the orifice(s). In the first generation design, this high voltage spark is initiated by the use of a third external trigger electrode as seen in Figures 1.2, 2.2, and 2.4. Subsequent studies on SparkJet efficiency (Haack et al. 2011) reveal that initiating the electrical discharge through the use of an integrated pseudo-series trigger as opposed to an external trigger increases the efficiency from 20-30% to 70% for an energy ratio,  $Q/E$ , near 10. The source of the series trigger spark comes from the anode and cathode of the sustain electrodes and eliminates the need for a third trigger electrode. This modification simplifies SparkJet construction and allows for an increase in the electrode tip gap distance. A larger electrode tip gap distance increases the operating efficiency by converting a larger amount of electrical energy to thermal energy. The surface area of the arc column between the electrodes is greater than with the external trigger and interacts with a larger percentage of the surrounding air, thus transferring more energy to the surrounding air. Figure 2.6 shows three operating efficiency curves as a function of the energy ratio,  $Q/E$ , and represents three different electrode gap distances. The operating efficiency decreases as  $Q/E$  increases, and the greatest effect of a larger gap distance on efficiency can be seen occurring around  $Q/E = 10$ . The increase in efficiency results from the fact that a lower capacitance or capacitor voltage could be used, which decreases the power requirement while obtaining results similar to those obtained from the externally triggered SparkJet. Another benefit of the increased gap distance is that the electrode tips are exposed to a lower average temperature and are less likely to experience thermal oxidation and thermal runaway. This increases the survivability and reliability of the electrodes as discussed in Haack et al. (2011)

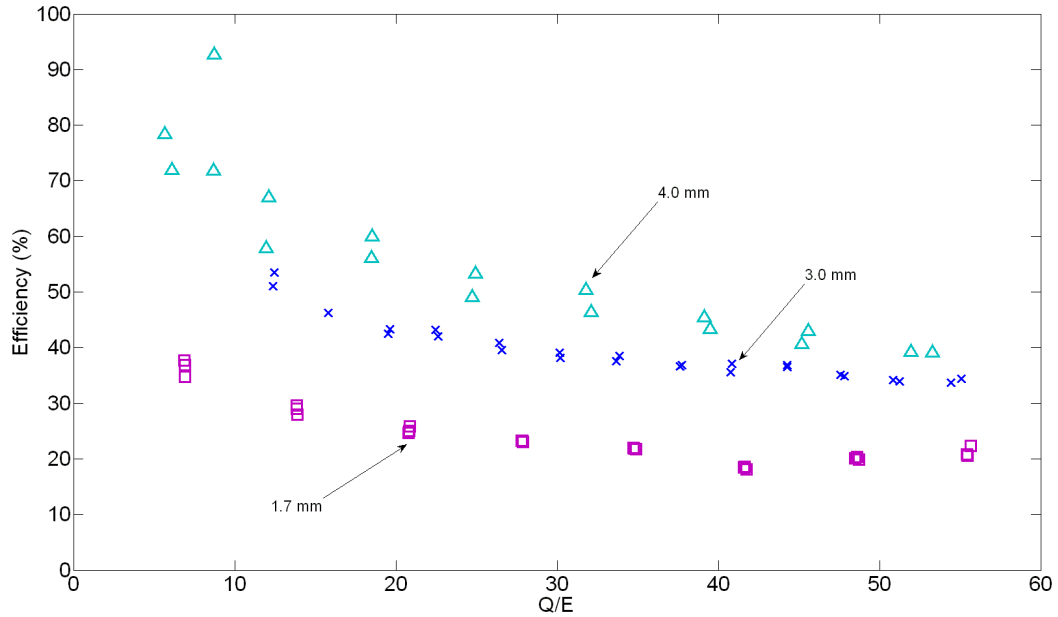


**Figure 2.6:** Operating efficiency with pseudo-series trigger mechanism.

#### 2.2.4. SJA with Cavity Refill Supply

One of the operating limitations of the SparkJet actuator is the time required for the cavity to ingest ambient air, i.e. to ‘refill’. Sufficient time must elapse for the cavity to be refilled by the ambient air after the high pressure discharge through the orifice(s) to ensure maximum momentum throughput when the subsequent discharge occurs. An additional SJA design that was developed and characterized using LBMS incorporates an air supply to allow for forced cavity refill. This non-ZNMF pulsed actuator was specifically developed for supersonic applications that require not only a large dynamic operating range, but also a sustainable high-momentum throughput greater than what the ZNMF version may be capable of producing at high operating frequencies (kHz). The forced cavity refill may, in principal, reduce the refresh time by supplying the cavity with compressed air. A photograph of this model is included in Figure 1.3. The actuator utilizes a Swagelok one way valve that connects to a 3 mm steel tube and ends at a 2 mm through hole to the SparkJet cavity. The one way valve was utilized to ensure that the pressure created from the electrical discharge does not flow back to the air refill source. A Cambell Hausfeld model FP202800 air compressor was used as the air supply. Air was supplied to the cavity at pressures of 1.4 psig and 3 psig to compare the effects of

different air supply pressures on momentum throughput. An Omega model FMA-5610-ST flow meter was used to measure the volumetric flow rate of the air entering the actuator. The actuator was triggered at 500, 700, and 1000 Hz and schlieren images were compared between the first and last discharge in a sequence of ten discharges. A PCB dynamic pressure sensor model 105C22 with a PCB model 482C signal conditioner was mounted in the cavity of the SparkJet to qualitatively verify that the actuator was reliably discharging at these higher frequencies. The sensor was mounted such that the face of the sensor was recessed to place protective insulating material over the sensor face without intruding on the cavity volume.

#### **2.2.5. Wind Tunnel Tests – SJAs and Model**

The SparkJet actuator was incorporated into a modular test bed integrated into the tunnel ceiling and subsequently tested in a Mach 1.5 crossflow. The actuator module used in wind tunnel testing consists of three externally triggered SparkJet assemblies. Each assembly consists of an electrode set (two parallel tungsten sustain electrodes and a trigger electrode) inside of a single 356 mm<sup>3</sup> cavity with four 400 µm diameter orifices. The resulting array is comprised of twelve 400 µm spanwise orifices spaced 2 mm apart (center-to-center). The actuator, the three electrode assemblies, and the location of the actuator in the wind tunnel can be seen in Figure 2.7. To install the SparkJet array, a single Macor block (Figure 2.8) was designed to hold the three electrode assemblies. Each electrode assembly consists of a cylindrical Macor piece with two axial holes spaced 0.7 mm apart (edge-to-edge) through which the tungsten electrodes slide such that the electrode tips are in the center of the cavity. The trigger wire is fed through a small hole in the side of the cavity and secured in place with epoxy. When installed in the upper test section lid, the cavities are closed with the 12 orifices being the only opening between the SparkJet cavities and the external flow. The 12 orifices are oriented normal to the incoming crossflow. Although not shown here, the REM actuators were also installed and tested at Mach 1.5 at a location similar to the SJA assembly. This allows for a reasonably direct comparison of the two actuation methods.



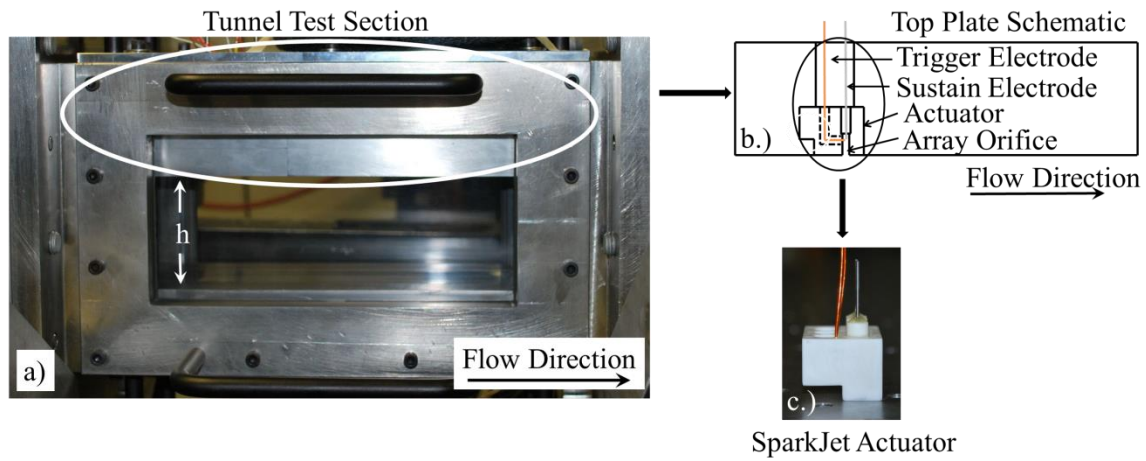


**Figure 2.7:** Actuator in wind tunnel; a) tunnel test section; b) tunnel ceiling; c) SparkJet actuator.

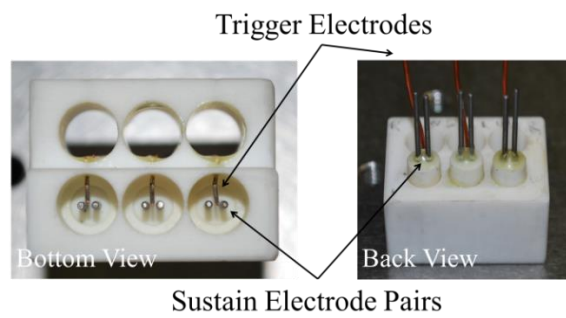


**Figure 2.8:** Bottom and rear views of the three-SJA assembly for wind tunnel tests.

### 3. Actuator Characterization under Quiescent Conditions

In this chapter we present the results from benchtop experiments that were used to characterize the flowfield produced by the SJA. As noted earlier, a number of design variants were examined through the course of this multi-year research; representative results from most of these will be discussed. As a comparison, selected, abbreviated results of the REM actuator are also included herein.

#### 3.1. Single-Shot Operation of the SJA

Testing and characterization of multiple SJA was performed to determine the impact of the important parameters on the flowfield produced by the actuator which ultimately impacts its efficacy in the control of high-speed flows. A range of orifice diameters, ambient conditions, refill air supply pressures, discharge frequencies, and trigger mechanisms were tested as shown in Table 3.1. The cavity volume of all of the actuators is 356 mm<sup>3</sup> and all of the benchtop images were taken using the LBMS system shown in Figure 2.1.

**Table 3.1:** SparkJet operating parameters

	<b>1 mm Orifice Diameter</b>	<b>400 <math>\mu</math>m Orifice Diameter</b>	<b>800 <math>\mu</math>m Orifice Diameter</b>
<b>Number of Orifices</b>	1	4	4
<b>Ambient Test Conditions</b>	Atmospheric	Atmospheric, Sub-Atmospheric (60 kPa)	Atmospheric
<b>Refill Supply Pressure (kPag)</b>	-	0, 10, 20	0, 10, 20
<b>Discharge Frequency (Hz)</b>	1	1, 500, 700, 1000	1, 500, 700, 1000
<b>Trigger Type</b>	External	External, Pseudo-Series	Pseudo-Series

##### 3.1.1. Single Orifice SJA – Atmospheric Conditions

Instantaneous schlieren images of a single 1 mm orifice SparkJet actuator operating at atmospheric conditions can be seen in Figure 3.1. The temporal evolution of the SparkJet flow features were examined by acquiring images where the time delay between the

SparkJet electrical discharge and the light source trigger was progressively varied. The images shown in Figures 3.1, 3.3, 3.4, and 3.5 are of the flowfield created by a *SJA using an external trigger* (as opposed to the pseudo-series trigger). The orifice diameter is marked by the white dashed lines in all of the images. In Figure 3.1, many of the principal features have also been indicated on this series of images. Two key features present in this flowfield are the initial blast wave and the jet front shown at a time delay of 8  $\mu\text{s}$ . Interestingly, a secondary blast wave can also be seen starting at a time delay of 10  $\mu\text{s}$  propagating with a velocity higher than the first. As a result, it coalesces with the initial blast wave  $\sim 16 \mu\text{s}$  after the SparkJet is discharged. A thermal or heat plume can be seen in all of the images in Figure 3.1 and is believed to be due to the heat transfer from the electrical discharge conducting through the Macor actuator lid and convecting into the ambient surrounding air. The actuator lid has a thickness of 1 mm and an internal diameter of 7.5 mm, where the inner diameter of the lid is marked in the images corresponding to time delays between 20 and 26  $\mu\text{s}$  by the solid white lines and arrows. The images reveal that the diameter of the heat plume (5 mm) is slightly smaller than the internal lid diameter (7.5 mm) and larger than the orifice diameter (1 mm).

A bright white feature is also seen just above the orifice in images corresponding to time delays between 8 and 16  $\mu\text{s}$ ; this is assumed to be the plasma discharge due to the electrical breakdown between the SparkJet electrodes. The diameter of the plasma discharge is geometrically similar to the SparkJet orifice diameter and smaller than the jet-front diameter. The propagation of the plasma discharge away from the actuator stays relatively constant when compared to the blast waves and jet front. The effect of the “plasma plume” on the flowfield is difficult to determine from these images because of its tendency to saturate the pixels in the images. Examining this interaction requires additional numerical/analytical studies supported by experiments which attempt to distinguish between the plasma plume and the subsequent jet exhaust. The images corresponding to time delays between 20 and 26  $\mu\text{s}$  show the propagation of the jet front and coalesced blast wave away from the actuator.

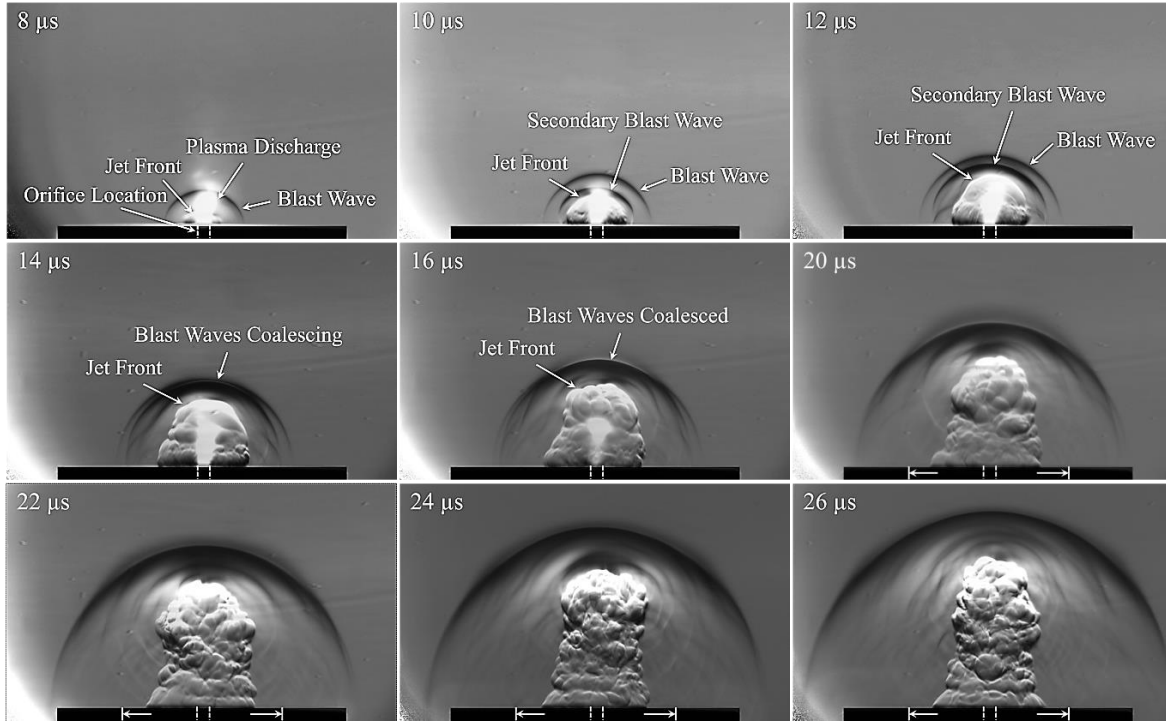


**Figure 3.1:** Time delayed schlieren images of the single 1 mm orifice SparkJet exhaust at atmospheric conditions.

The blast wave and jet front propagation velocities are plotted versus the time after discharge in Figure 3.2. These were carefully measured from the time-conditioned images using a calibration image and the known time delays between images. The maximum jet front and blast wave velocities were measured to be 310 m/s and 410 m/s, respectively in the early stages of the SJA operation. An important feature to note is how rapidly the SJA flowfield develops after discharge where the maximum velocity is reached in less 15  $\mu$ s under ambient conditions. The very fast response and the high initial velocity are attractive for high-speed flow control applications. The velocities of the jet front and blast wave decay as the time increases from the initial SparkJet arc discharge, as expected. A slight increase in velocity occurs at approximately 20  $\mu$ s and is seen as a small bump in Figure 3.2, it is thought to be caused by the interaction of reflected blast waves. (Foster et al. 2011)

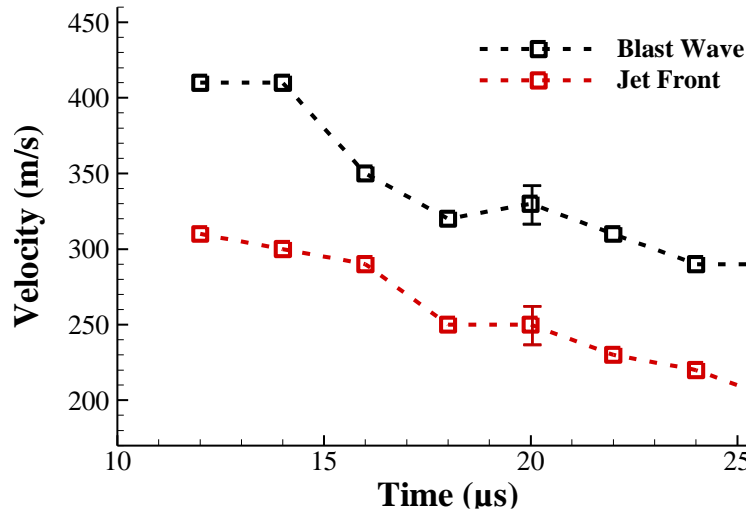


**Figure 3.2:** Blast wave and jet front propagation velocities at atmospheric conditions.

The exhaust jet from the SJA at much longer time delays is shown in Figure 3.3. This jet and the thermal plume of the cavity is still sustained at these large time delays and benchtop studies have revealed that the presence of the jet can be seen up to two milliseconds after the initial discharge. Analytical and experimental results of Haack et al. (2010) suggest that the pressure in the cavity of the actuator settles to atmospheric pressure roughly 200  $\mu$ s after the initial discharge. The features observed 200  $\mu$ s after the initial discharge may be solely related to the heat plume created by the intense electrical breakdown and unrelated to the high momentum jet flow created by the actuator. However, the results shown here up to a time delay of 550  $\mu$ s pose a possible limit on the maximum frequency that these actuators can be operated at while delivering maximum momentum throughput without an external supply.

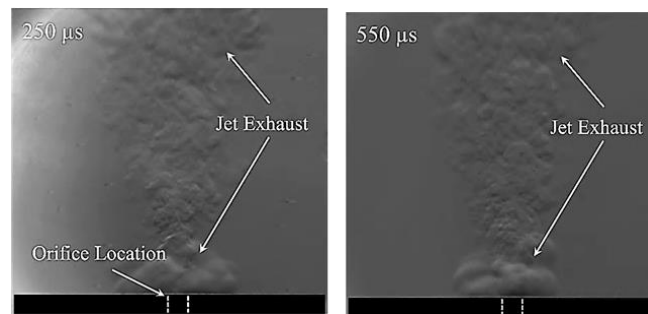


**Figure 3.3:** 250  $\mu$ s and 550  $\mu$ s time delayed schlieren images at atmospheric conditions.

### 3.1.2. Four Orifice SJA – Atmospheric Conditions

Schlieren images of a first generation, four orifice SparkJet array operating at atmospheric conditions are shown in Figure 3.4 (Foster et al. 2011). These images show the same key features of an initial blast wave and jet front as those in Figure 3.1 for the single orifice SJA; however, additional features including reflected blast waves and a second jet front are observed at  $\sim 22 \mu\text{s}$  delay. These features are labeled in Figure 3.4b. The cause of the secondary jet front and blast waves is suspected to be due to reflections of the initial blast wave in the cavity. An examination of the overall images at time delays of 18 through  $40 \mu\text{s}$  reveals that the four jets in the array have propagated nearly the same distance. However, the spherical blast waves of the two outside jets at time delays of  $10 \mu\text{s}$  and  $12 \mu\text{s}$  have not propagated as far away from the actuator as the blast waves of the two center jets. Another interesting flow feature is revealed at a time delay of  $40 \mu\text{s}$  and consists of a large density gradient across the two center jets in the array. This may be caused by the presence of high temperature exhaust gases issuing through the center orifices.

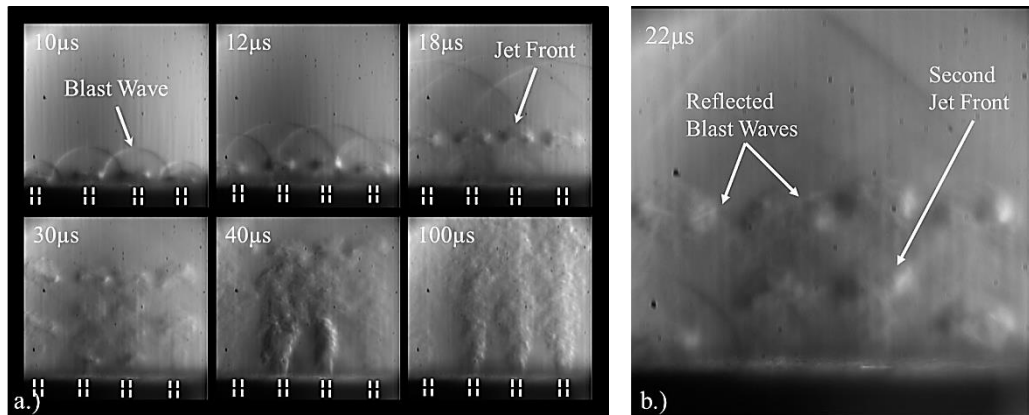


**Figure 3.4:** Time delayed schlieren images of the SparkJet exhaust at atmospheric conditions; a)  $10 \mu\text{s}$ - $100 \mu\text{s}$  time delays; b)  $22 \mu\text{s}$  time delay showing reflected shocks and second jet front.

### 3.1.3. Four Orifice Array Testing at Sub-Atmospheric Conditions

Time delayed schlieren images were also acquired for a four-orifice SparkJet array operating at a pressure of 60 kPa in the custom built vacuum chamber described in chapter 2. This allowed for the actuator to be tested at ambient pressures similar to those

encountered during wind tunnel testing and those encountered during high altitude flight; it also allowed for a direct comparison with the actuator operating at atmospheric conditions. The SJA was visualized at increasing time delays starting at a delay of 6  $\mu\text{s}$ , which is when the blast wave generated by the electrical discharge is first seen exiting from the orifice array. Flowfield images were captured up to a delay of 70  $\mu\text{s}$ . As before, the four orifices are marked by the white dashed lines in all of the images. Instantaneous images from several of these time delays are shown in Figure 3.5.

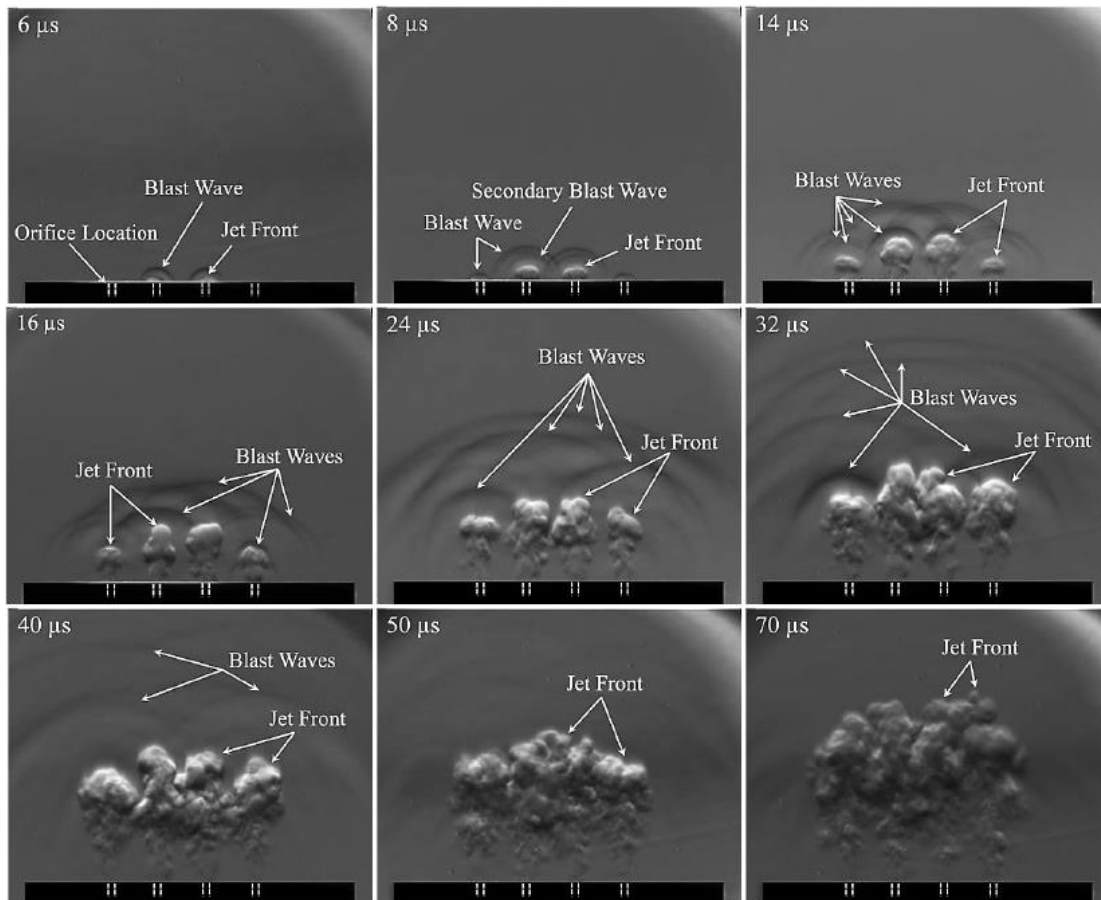


**Figure 3.5:** Time-resolved schlieren images of the four orifice SJA exhaust at 60 kPa.

Results of the sub-atmospheric testing of the four-orifice actuator array reveal flow features similar to those observed at atmospheric conditions including an initial blast wave and jet front. The presence of multiple blast waves is also seen in both atmospheric and sub-atmospheric testing; however, there are some differences as well. A secondary blast wave can be seen in the image corresponding to a time delay of 8  $\mu\text{s}$ , similar to the

secondary blast wave seen in the single-orifice SparkJet tested at atmospheric conditions. Note that the secondary blast wave is not seen in the four-orifice array tested at atmospheric conditions. The occurrence of multiple blast waves in these images is believed to be due to reflections of the original blast wave in the cavity. Furthermore, the high-density gradient of the center two jets is not present at a time delay of 40  $\mu\text{s}$  in sub-atmospheric conditions as was seen in atmospheric conditions. Additionally, the four jets in the array do not propagate the same distance with respect to one another as was observed at atmospheric conditions. The two center jets are at a further distance away from the actuator than the two outside jets during sub-atmospheric testing, but they do begin to converge 70  $\mu\text{s}$  after the SparkJet has discharged.

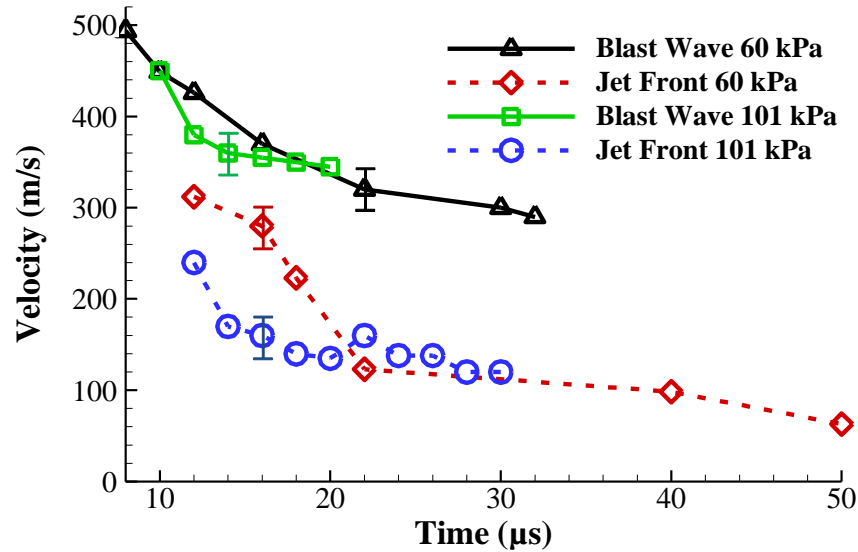


**Figure 3.6:** Blast wave and jet front velocity measurements.

The propagation speeds of the initial blast wave and jet front were measured at atmospheric and sub-atmospheric conditions and are shown in Figure 3.6. For both the cases, the initial blast wave is followed by a jet front which propagates at a velocity lower than the blast wave. Velocities decay as they travel away from the actuator at both sub-atmospheric and atmospheric conditions. The velocities of the blast wave for both conditions at a time delay of 10  $\mu\text{s}$  were found to be 450 m/s. The jet front velocities at atmospheric and sub-atmospheric conditions at a time delay of 12  $\mu\text{s}$  were found to be 240 m/s and 310 m/s, respectively. These results indicate that the potential control authority of the SparkJet may increase at lower ambient pressures encountered in wind



tunnel tests and/or flight conditions at high altitudes due to the increased jet front velocity. However, a lower ambient pressure may also result in a lower density jet created by the SparkJet and may counteract the benefit of an increase in jet velocity.

#### 3.1.4. Four Orifice Array Testing at Sub-Atmospheric Conditions

The blast wave and jet front propagation speeds of a four orifice SJA employing an external trigger were compared to a similar actuator that utilized a pseudo-series trigger. The results are shown below in Figure 3.7. The average velocity of the blast wave created by the actuator employing the pseudo-series trigger is roughly 60 m/s greater for time delays between 12 and 20  $\mu$ s than the blast wave generated by the actuator employing an external trigger. The jet front velocity of the actuator that incorporates a pseudo-series trigger is also increased when compared to the actuator that employs an external trigger. While the velocity differences are not very drastic, the findings do confirm that the efficiency of the actuator is increased by using a series trigger mechanism. This is further proven by the fact that roughly half of the capacitance was stored across the sustain electrodes in the actuator that employs the pseudo-series trigger, as discussed in §2.1, while producing a flowfield with higher velocities present.

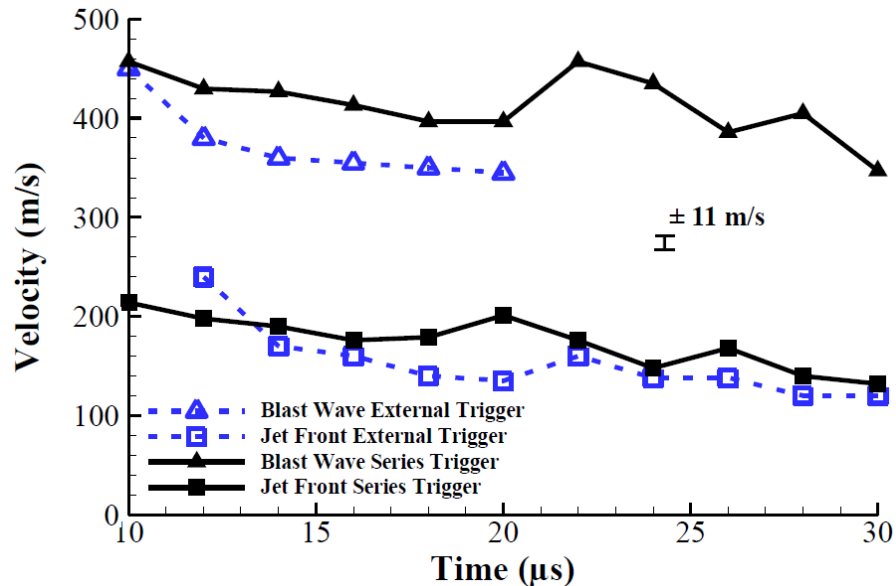


**Figure 3.7:** Blast wave and jet front velocity measurements.

### 3.1.5. Four Orifice 400 $\mu\text{m}$ SJA with Pseudo-Series Trigger - Atmospheric Conditions with Various Active Refill Supply Pressures

**No Refill Supply** - As discussed earlier, the effect of air supply pressures on the momentum throughput of the SparkJet actuator was investigated in benchtop testing. Air was supplied to the cavity of the actuator at pressures of 1.4 and 3 psig. The baseline case, without an external air supply, was first examined and images of the SJA operating at various time delays is shown below in Figure 3.8. These images depict similar features, including blast waves and jet fronts, as those seen in previous benchtop studies. While secondary jets fronts and blast waves can be seen in the images as the time delay is increased, the blast waves do not coalesce as was observed for the single orifice actuator discussed earlier. The heat plume generated by the SparkJet is seen exiting the orifices of the actuator up to a time delay of 750  $\mu\text{s}$ .

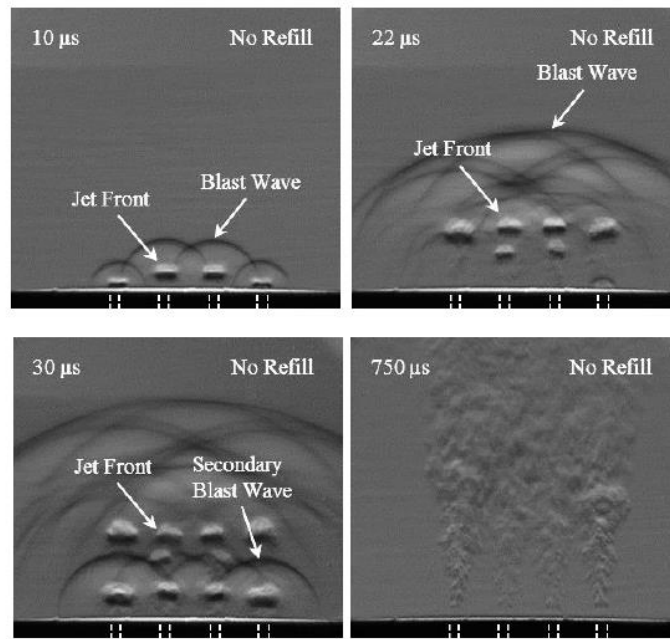


**Figure 3.8:** Time delayed schlieren images of the 400  $\mu\text{m}$  four orifice SparkJet exhaust with no refill supply.

**With 1.4 psig Refill Supply** - The effect of supplying the cavity of the SparkJet actuator with air at a pressure of 1.4 psig can be seen in Figure 3.9. The volumetric flow rate exiting through the orifices was measured using an Omega model FMA-5610-ST flow meter, and the corresponding steady jet flow velocity was estimated to be 23 m/s at this

refill supply pressure. The influence of the 1.4 psig refill supply pressure on the flowfield is minimal, and similar features as those seen in Figure 3.8 with no refill supply can be seen in Figure 3.9.

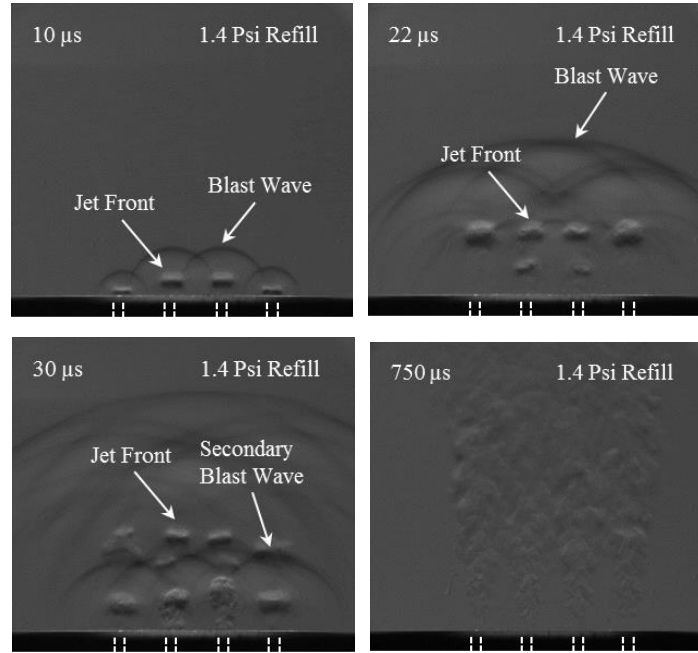


**Figure 3.9:** Time delayed schlieren images of the 400  $\mu\text{m}$  four orifice SparkJet exhaust with 1.4 psig refill.

***With 3 psig Refill Supply*** – Similarly, the effect of supplying the SJA actuator with air at a pressure of 3 psig was also investigated. The corresponding steady jet flow velocity was calculated to be 66 m/s at this refill supply pressure. Schlieren images taken during these test conditions are shown in Figure 3.10. The shape of the blast wave is altered by the air supply as can be seen at time delays of 10, 22, and 30  $\mu\text{s}$ . A comparison of these images with those corresponding the 1.4 psig supply reveals that the coherence of the exhaust jet is measurably reduced by the presence of the 3 psig refresh supply, as one may expect.

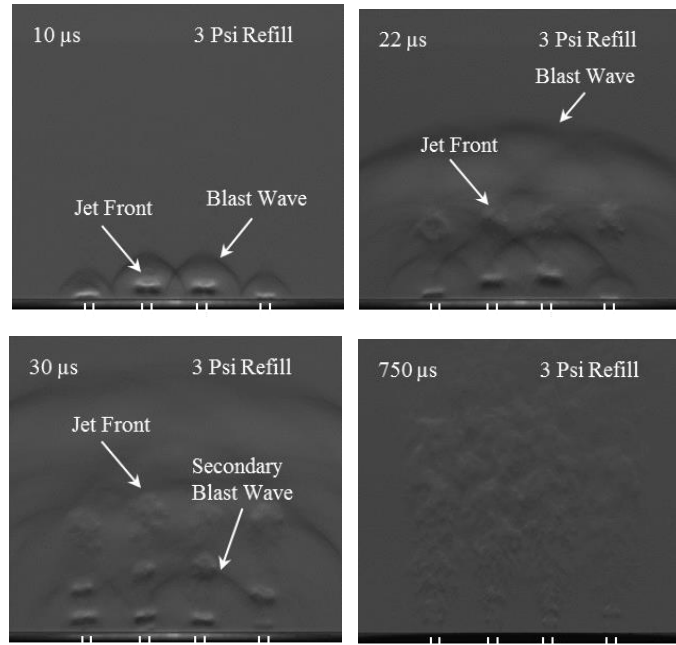


**Figure 3.10:** Time delayed schlieren images of the 400  $\mu\text{m}$  four orifice SparkJet exhaust with 3 psig refill.

A compilation of instantaneous schlieren images taken of the exhaust created by the 400  $\mu\text{m}$  four orifice actuator utilizing an active refill supply can be seen in Figure 3.11. The refill supply pressure value and time delay increase from left to right and top to bottom in the images, respectively. A reduction in the coherence of the blast waves as the refill supply pressure increases occurs and can be seen in the images.

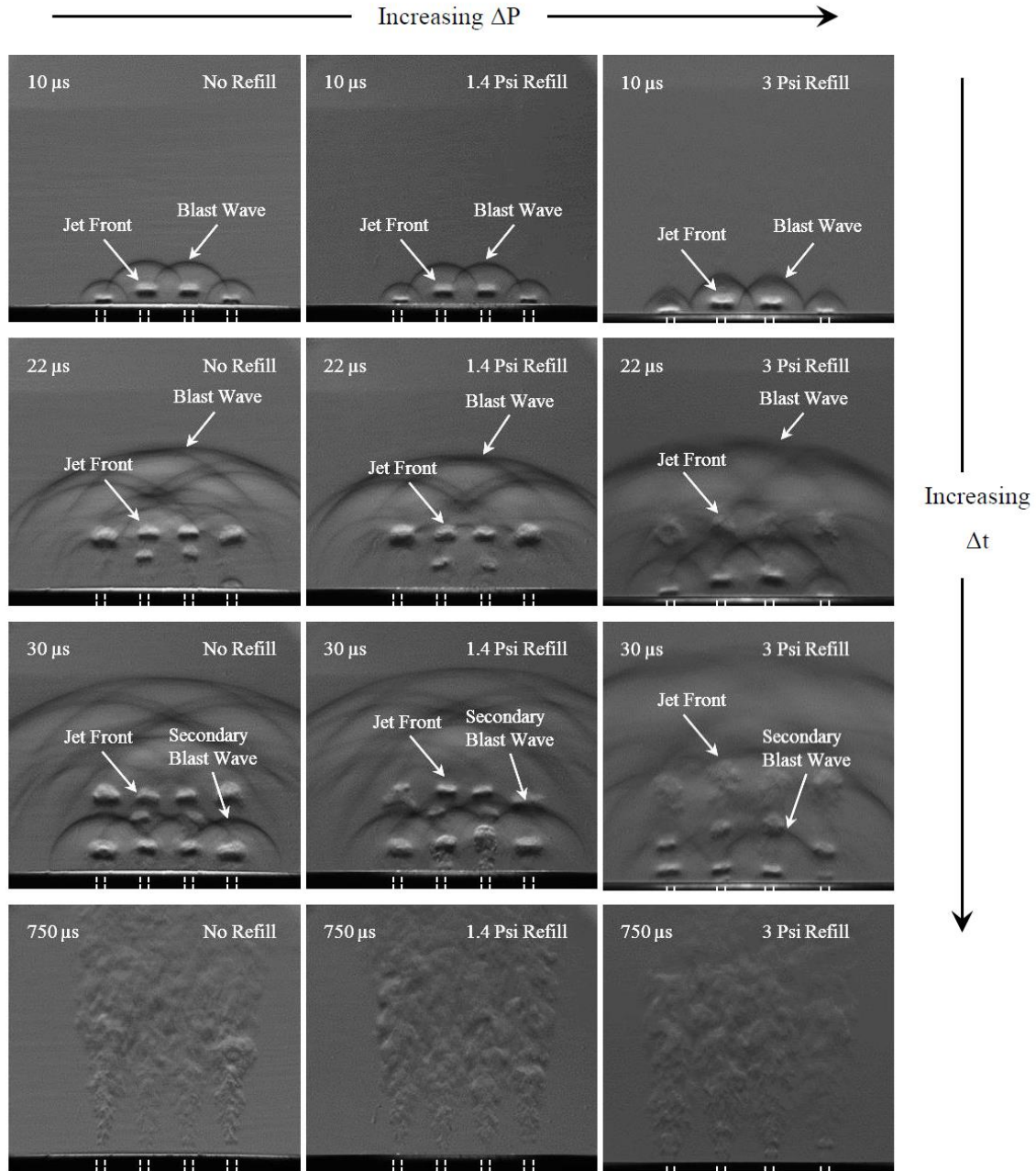


**Figure 3.11:** Time delayed schlieren images of the 400  $\mu m$  four orifice pseudo-series triggered SJA with various refill supply pressures.

The propagation speeds of the blast waves and jet fronts were measured using the technique discussed in §3.1.1 and compared for different refill supply pressures. Similar jet front and blast wave velocities as those measured before were found. The relation between the blast wave velocity and refill supply pressure is unclear at this point; the

trends corresponding to different air supply pressures cross and do not reveal a clear correlation between the blast wave velocity and refill air supply pressure. There is a more distinct correlation between the refill air supply pressures and jet front velocities. An overall assessment of Figure 3.12 reveals that an increase in cavity refill supply pressure results in an increase in jet front velocity, at least for time delays between 12 and 20  $\mu\text{s}$ . As an example, at a time delay of 12  $\mu\text{s}$ , the jet front velocity corresponding to no cavity refill supply is measured to be 198 m/s. At the same time delay at a refill supply of 1.4 and 3 psig, the jet front velocities are measured to be 247 and 283 m/s, respectively.

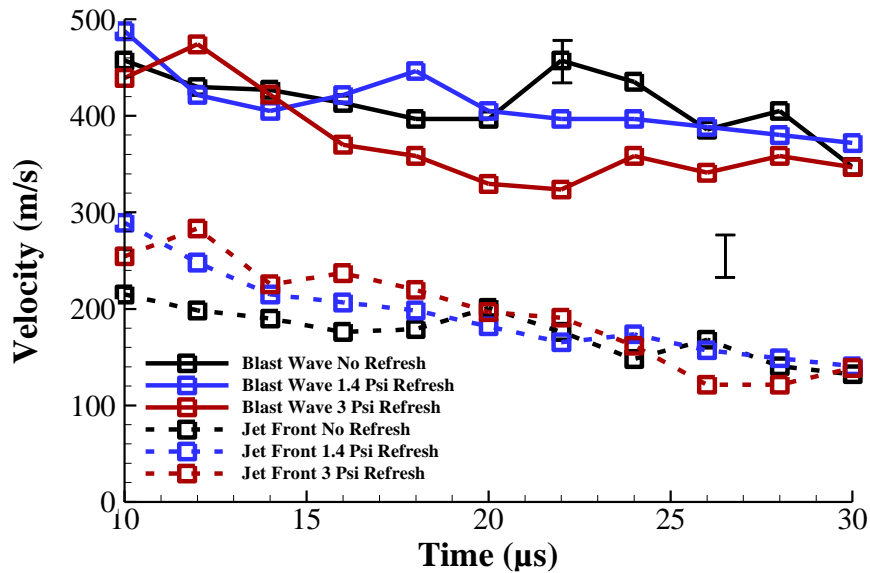


**Figure 3.12:** Blast wave and jet front velocity calculations of four 400  $\mu\text{m}$  orifice actuator with various refill supply pressures.

### 3.1.6. Four Orifice 800 $\mu\text{m}$ SJA with Various Active Refill Supply Pressures

In a manner similar to the previously discussed case, the effect of varying the cavity supply pressure for an SJA with larger, 800  $\mu\text{m}$  diameter orifices was also examined. The effect of varying the supply pressure on the flowfield with 800  $\mu\text{m}$  diameter orifices is similar to the flow from the 400  $\mu\text{m}$  diameter SJA. As in the smaller orifice case, a higher supply pressure alters shape of the blast waves and the jet fronts appear less coherent. Similar to Figure 3.11, a compilation of instantaneous schlieren images taken of the exhaust created by the 800  $\mu\text{m}$  four orifice actuator utilizing an active refill supply can be seen in Figure 3.13. These results follow the trends observed for the 400  $\mu\text{m}$  diameter SJA.

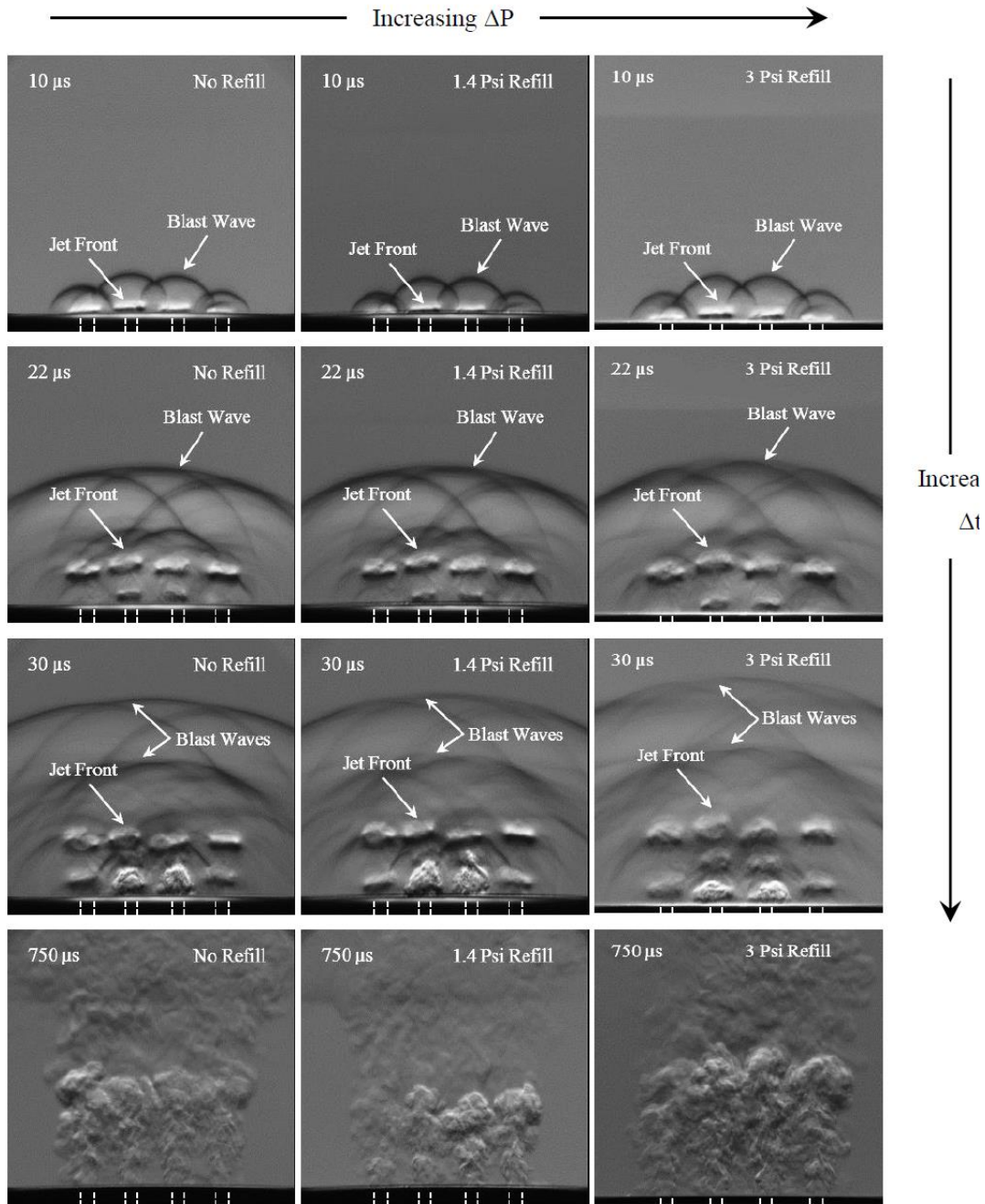


**Figure 3.13:** Time delayed schlieren images of the 800  $\mu m$  four orifice pseudo-series triggered SJA with various refill supply pressures.

### 3.1.7. Effect of Orifice Diameter on Flowfield Velocity

A plot showing the velocities of the jet fronts and blast waves created by a four orifice actuator with 400  $\mu m$  diameter orifices and an actuator with 800  $\mu m$  diameter orifices is

contained in Figure 3.14. The data presented corresponds to the case of no refill supply for both of the actuators. The velocities of the flow features generated by the actuator with 400  $\mu\text{m}$  diameter orifices are higher than those generated by the actuator that utilizes 800  $\mu\text{m}$  diameter orifices. At a time delay of 10  $\mu\text{s}$ , the blast wave created by the 400  $\mu\text{m}$  diameter orifice actuator is roughly 25 m/s faster than the blast wave created by the 800  $\mu\text{m}$  diameter orifice actuator. The velocity of the jet front generated by the 400  $\mu\text{m}$  diameter orifice actuator is roughly 100 m/s faster at this time delay than the velocity of the jet front created by the 800  $\mu\text{m}$  diameter orifice actuator. This trend is somewhat expected, since at similar operating conditions, the same amount of energy is deposited in the cavity by the spark, thus requiring a higher momentum jet efflux for a smaller diameter orifice. Other aspects, such as higher losses for smaller diameter orifices and the ingestion time (for pulsed mode) that may have an opposite effect. However, these were not investigated experimentally, albeit they are expected to be second order effects.

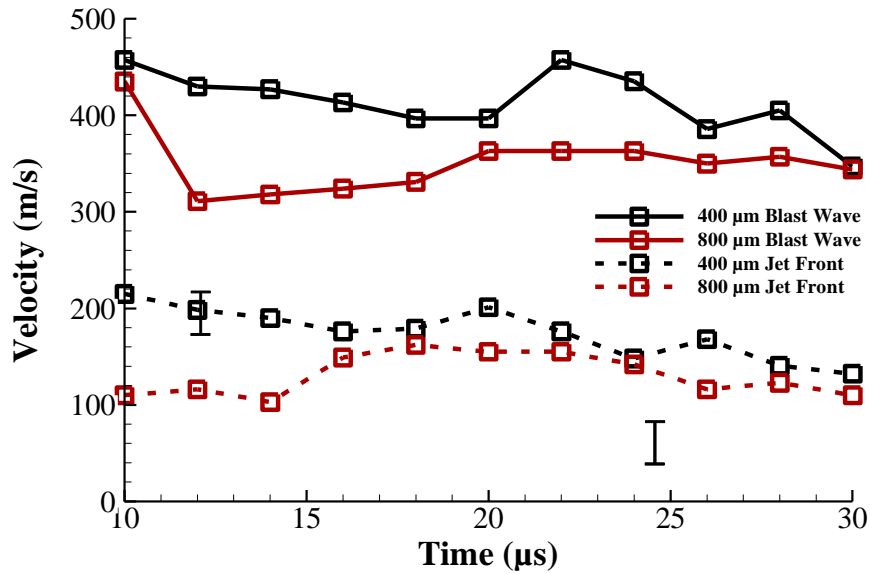


**Figure 3.14:** Comparison of orifice diameter on jet front and blast wave velocities.

### 3.2. Burst Mode Operation of the SJA

In most practical applications, SJA (and most pulsed actuators) must operate at high repetition rates, where the actuator frequency is dictated by the target flow to be controlled. As such, we examined the SJA operation where it is repeatedly pulsed at a high frequency. However, due to thermal management constraints, i.e. heating of the SJA



hardware, the actuator can only be pulsed in short bursts. The SparkJet actuator utilizes a burst mode firing sequence to operate up to a kilohertz for a fixed number of discharges. Similar to the single shot results discussed in §3.1, schlieren images for two SJA designs were acquired for burst mode operation. Both actuators utilize a pseudo-series trigger mechanism and have four orifices, the first with 400  $\mu\text{m}$  diameter orifices and the second 800  $\mu\text{m}$  diameter orifices. The cavity of each actuator was supplied with air at 1.4 and 3 psig during the burst mode operation to determine if it has any effect on the refresh time and hence actuator performance. Discharge frequencies of 500, 700, and 1000 Hz were examined for each SJA. In the following, we only discuss results of burst mode operation for the 400  $\mu\text{m}$  SJA as this is the actuator subsequently tested in the wind tunnel. Details of the 800  $\mu\text{m}$  SJA burst mode performance can be found in Emerick (2013).

### **3.1.1. Burst Mode Discharge Reliability**

Initial testing of the SJA consisted of discharging the actuator 100 times at frequencies of 500, 700, and 1000 Hz. A PCB pressure transducer was mounted near the cavity of the actuator to monitor the discharge reliability. The pressure measurements also revealed that the actuator was reliable and consistent during the first 10 to 15 discharges in the firing sequence, and that consistency and reliability decreased thereafter. For this reason, the firing sequence of the actuator was reduced from 100 discharges to 11. A plot of the data collected using the pressure transducer is shown in Figure 3.15. The blue spikes on the plot confirm that the actuator discharged during the firing sequence. The dashed red lines on the plot show when the actuator misfired. The plot also shows that the actuator was 100 percent reliable during the first 13 discharge in the firing sequence. A second plot, shown in Figure 3.16, shows the data from the pressure transducer used during an 11 discharge firing sequence, confirming the reliability of the actuator during this firing sequence.

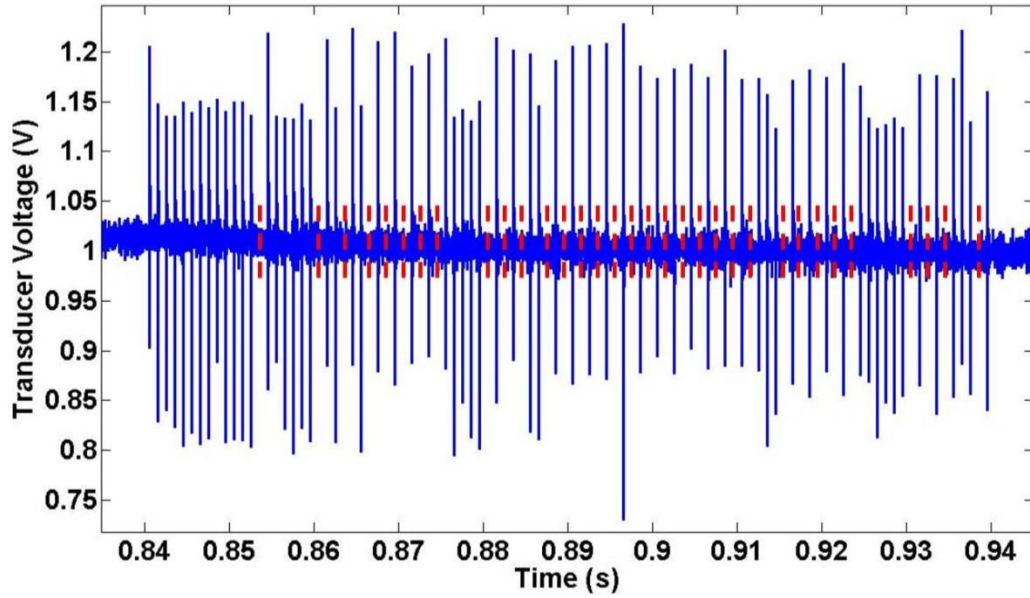


**Figure 3.15:** Pressure measurements to examine the reliability of the SparkJet actuator during a 100 discharge firing sequence at 1 kHz.

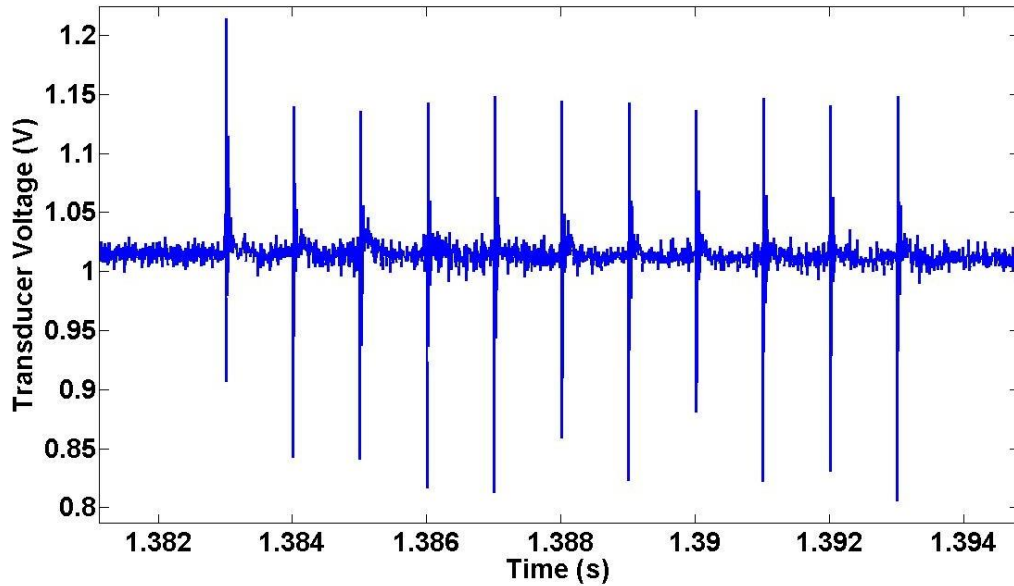


**Figure 3.16:** Qualitative data revealing the reliability of the SparkJet actuator during an 11 discharge firing sequence at 1 kHz.

### 3.1.2. 500 Hz operation with various refill supply pressures (400 $\mu\text{m}$ orifice)

The phase-conditioned schlieren images shown in Figure 3.17 compare the effects of different cavity refill supply pressures on the flowfield created by the four orifice (400

$\mu\text{m}$ ) SJA while discharging 11 times at a frequency of 500 Hz. The images capture the flowfield created by the 10th discharge in the firing sequence at time delays of 20, 22, and 24  $\mu\text{s}$  after the discharge initiation. The time delay after the initial energy deposition increases in the images from left to right, while the cavity refill supply pressure increases from top to bottom, similar to Figures 3.11 and 3.13.

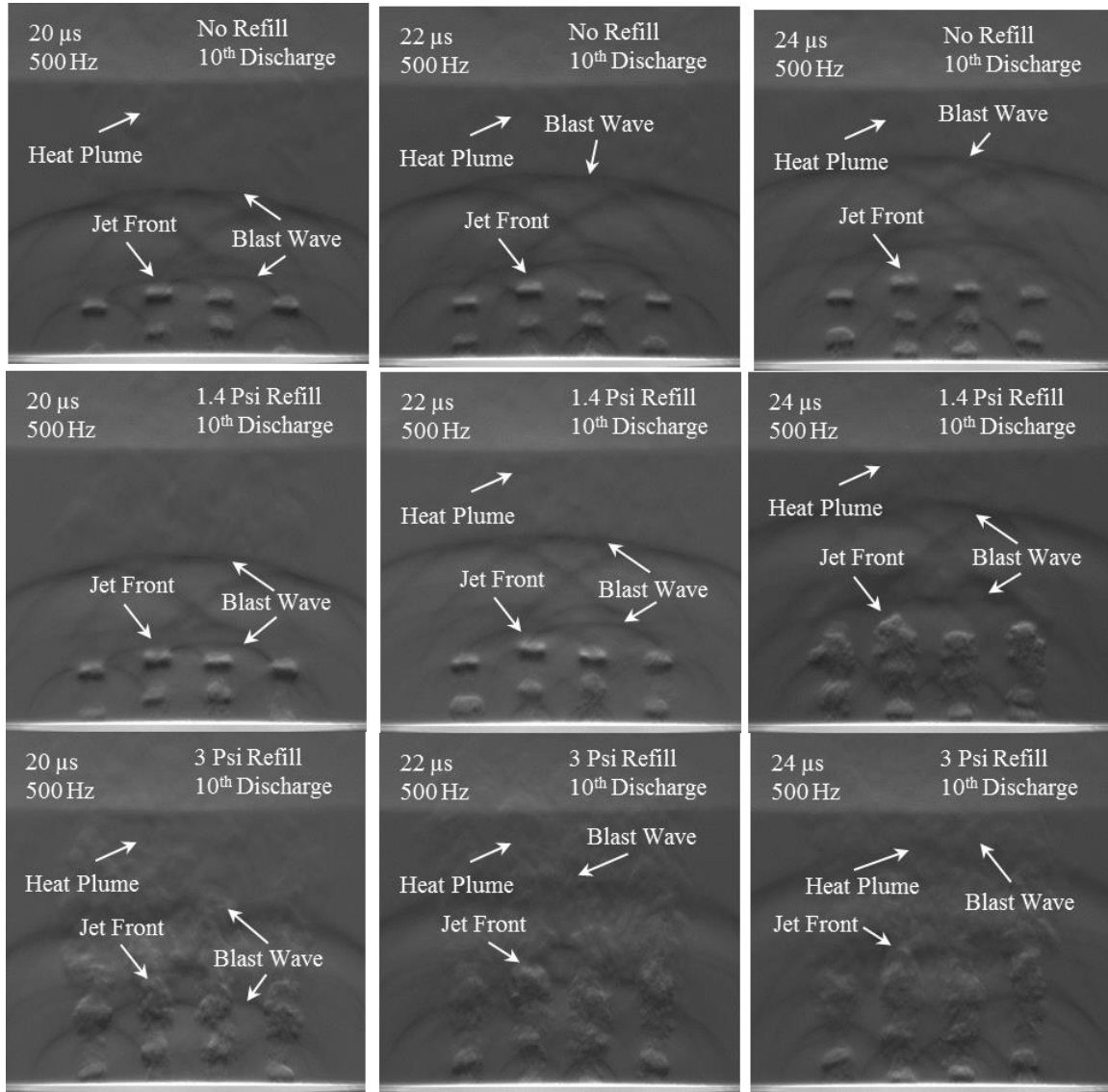


**Figure 3.17:** Burst mode operation of four 400  $\mu\text{m}$  SJA at 500 Hz with various cavity refill supply pressures.

The familiar features of blast waves and jet fronts are present in all of the images. A new feature observed during burst mode operation testing is the presence of a thermal plume. The thermal plume is created by the high frequency repetition of the intense heating of the air inside of the cavity. These results suggest that the accumulation of thermal energy in the burst mode may have an appreciable impact on the actuator throughput, especially if the burst mode involves a large number of pulses and/or is discharged at very high frequencies. The distinction between the effects of the jet flow and the effects of the thermal plume on the ambient fluid will have to be understood in a more comprehensive manner, through high-fidelity simulations and additional experiments, if this actuator is to be used for active flow control.

These schlieren images of the flowfield when there is no cavity refill supply define a baseline case for comparisons and contrasts to be made to the flowfield created by the actuator when a cavity refill supply pressure is present. A 1.4 psig cavity refill supply pressure causes an influence on the jet structure at a time delay of 24  $\mu$ s. The distinct sets of horseshoe vortical structures observed in the jet front when there is no cavity refill supply are altered by the addition of a cavity refill supply pressure. The additional presence of the cavity refill air is clearly seen being expelled from the orifices when the pressure is 3 psig. The presence of the blast wave is less dominant when the supply pressure is 3 psig than when there is no cavity refill supply pressure and the jet front and heat plume presence are intensified.

### **3.1.3. 700 Hz operation with various refill supply pressures (400 $\mu$ m orifice)**

The presence of jet fronts, blast waves, and a heat plume are present in the flowfield created by the SparkJet when operating in burst mode at 700 Hz. As before, the actuator was discharged 11 times during these tests and images of the flowfield created by the 10th discharge at time delays of 20, 22, and 24  $\mu$ s are shown in Figure 3.18. The stronger density gradient associated with the heat plume indicates that the intensity of the heat plume is increased in these images when compared to the images in Figure 3.17 when the actuator was operating at a frequency of 500 Hz. As previously discussed, the presence of the refill supply air alters the jet structure at supply pressures of 1.4 and 3 psig. The blast

waves are less distinct as the cavity refill supply pressure is increased, and they are also visually weaker when compared to the burst mode operation at 500 Hz.

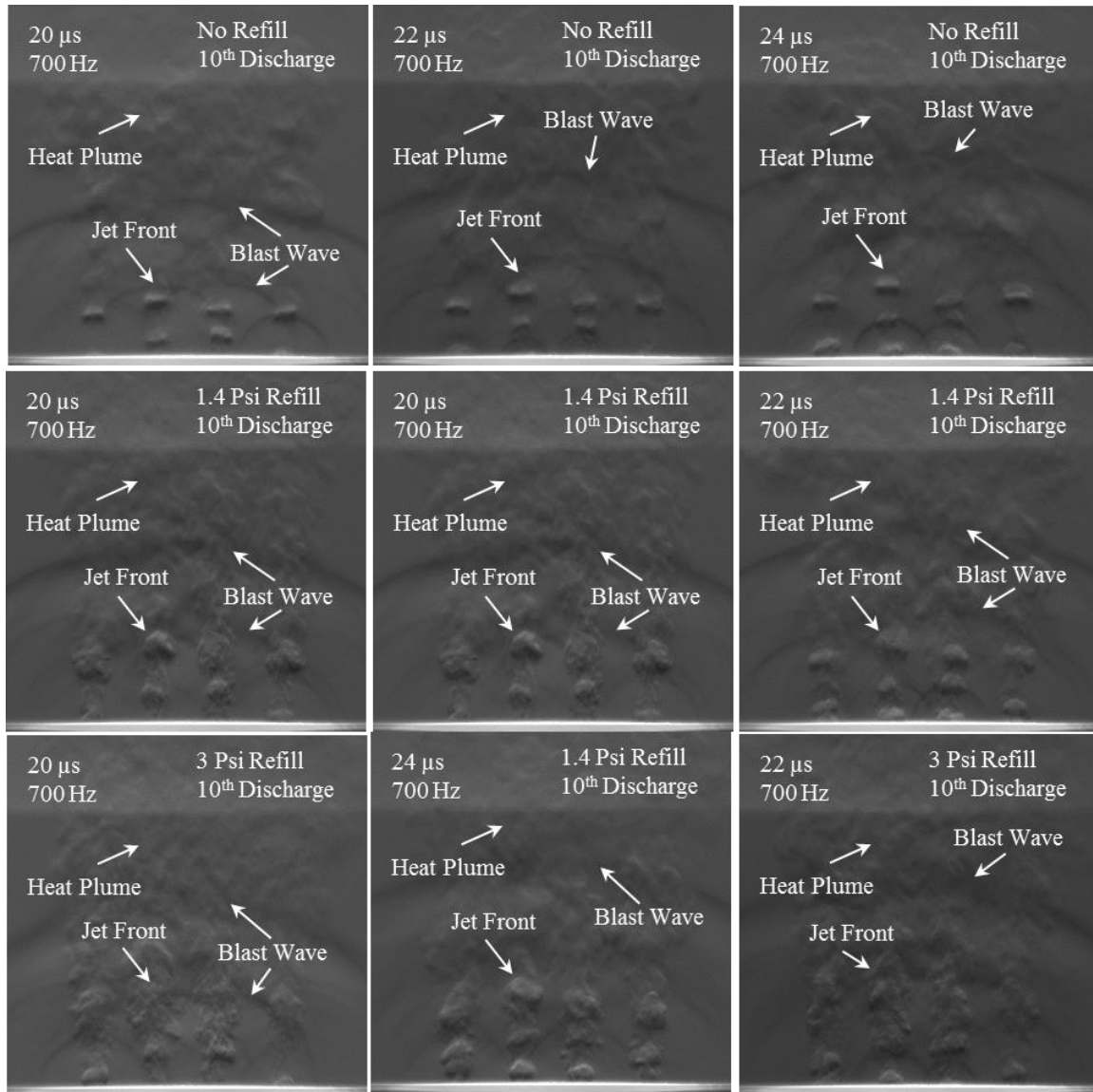


**Figure 3.18:** Burst mode operation of four 400  $\mu$ m SJA at 700 Hz with various cavity refill supply pressures.

#### 3.1.4. 1 kHz operation with various refill supply pressures (400 $\mu$ m orifice)

Images of the 10th discharge while operating at a frequency of 1 kHz in the firing sequence are shown in Figure 3.19. At this frequency, the jet structures for all refill air supply pressures do not contain the distinct vortical structures seen in Figures 3.17 and

3.18. There is also minimal difference in the flow dynamics between the cases of no refill supply and an air supply pressure of 1.4 psig. However, increasing the air refill supply pressure to 3 psig intensifies the presence of the jets and heat plume in the images.

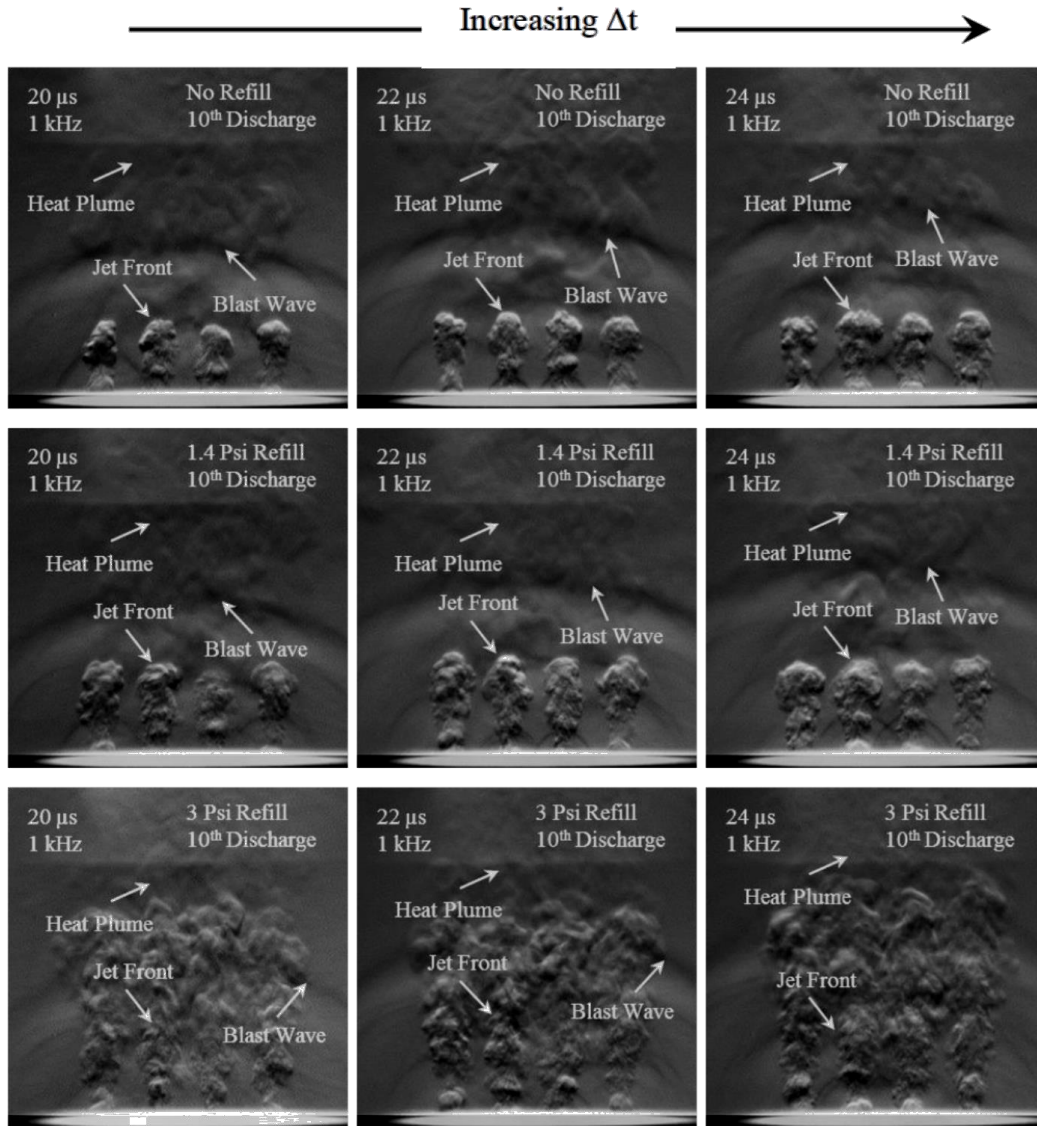
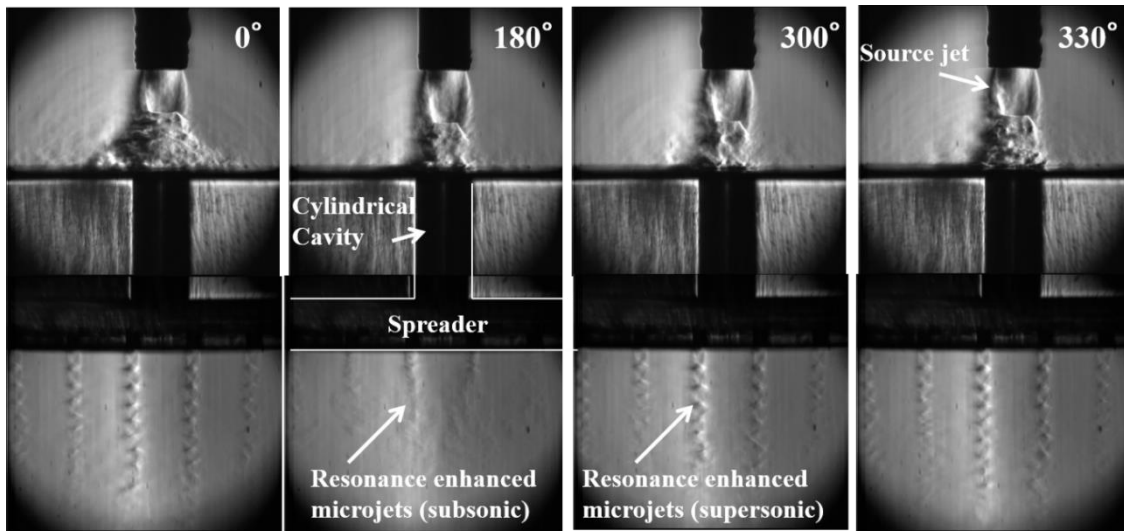


**Figure 3.19:** Burst mode operation of four 400  $\mu$ m SJA at 1 kHz with various cavity refill supply pressures.

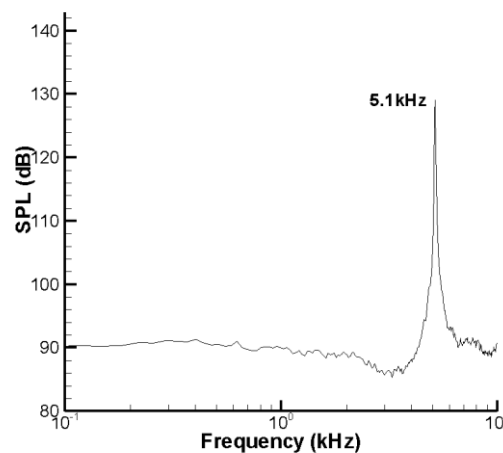
### 3.3. REM Actuator – Selected Results

Figure 3.20 shows typical phase-conditioned microschlieren images of a REM actuator flowfield, obtained using the laser based microschlieren system. These images show a

REM actuator pulsing at a frequency of  $\sim 5$  kHz, and clearly demonstrate the pulsing behavior of the microjets, which vary from supersonic to subsonic speeds throughout the various phases. During various portions of the actuator cycle, it can be seen that the microjets vary from low subsonic to highly underexpanded supersonic velocities. This variation in exit velocity occurs at the design frequency of  $\sim 5$  kHz. A near-field acoustic spectrum showing this actuator's frequency of  $\sim 5$  kHz can be seen in Figure 3.21. More details of this particular actuator design and its parametric studies are available in Solomon et al. (2010).



**Figure 3.20:** Phase conditioned microschlieren flow visualizations of a typical REM actuator flowfield. (Foster 2011)



**Figure 3.21:** Unsteady acoustic spectrum of a  $\sim 5$  kHz REM with 6 microjets. (Foster 2011)

Additional studies were performed with a simplified REM design such that comparisons with CFD simulations can be made. This simplified design has only one pulsed supersonic microjet. As a qualitative comparison to the experimental results, the density contours from the simulation are scaled and shown alongside phase-conditioned images from the LBMS system of the single orifice REM actuator. A sample of these results is shown in Figure 3.22 for a few select phases of the pulsed operation, which was at a frequency of 8.3 kHz. Details of this actuator's design, the simulations, and further comparisons can be found in Uzun et al. (Dec 2013).

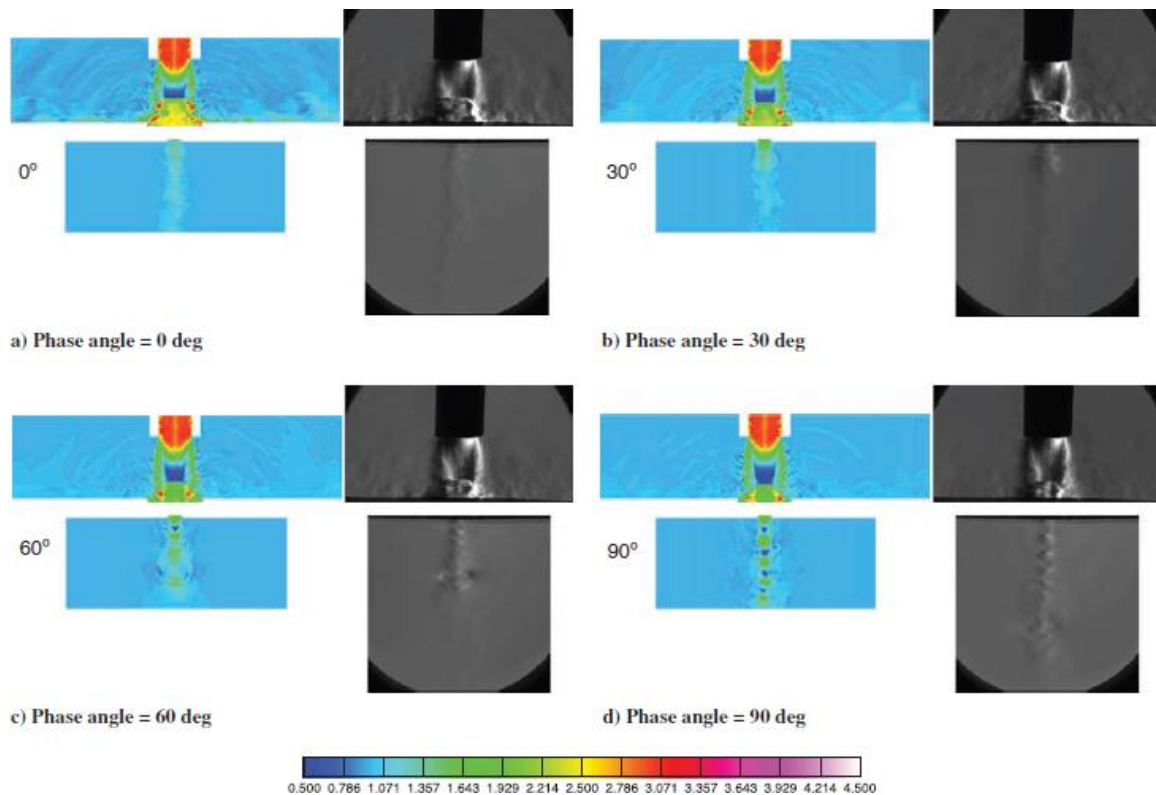


**Figure 3.22:** Qualitative comparison of density contours from simulation with experimental microschlieren images at representative phase angles. (Uzun et al. Dec 2013)



## **4. SJA Performance in Supersonic Crossflow (Tunnel Experiments)**

As noted earlier, the primary use for developing the SJA is for supersonic flow control applications. Towards this end, an SJA array was designed by JHU/APL to be tested in the supersonic wind tunnel at FSU. Representative results of this experimental study are discussed in this chapter where the flow, i.e. jets, produced by the actuator interacts with a supersonic freestream. The response of the supersonic crossflow as well as the actuator flow is characterized using time-resolved visualizations. All the experiments discussed here use an array consisting of three actuator modules, where each SJA module produces four 400  $\mu\text{m}$  jets for a total of twelve jets. More details on the SJAs used in the wind tunnel can be found in §2.2.5. Facility and diagnostic details are provided next, followed by results.

### **4.1. Tunnel Facility and Test Conditions**

The supersonic crossflow experiments were conducted at the supersonic wind tunnel facility (Figure 4.1) at the Florida Center for Advanced Aero-Propulsion (FCAAP) at Florida State University. The tunnel is supplied with dry, pressurized air from a 10  $\text{m}^3$  air tank at 13 MPa. Control of the air flow to the test section is maintained through the use of two inline valves, a Tescom<sup>TM</sup> dome regulator and a Fisher<sup>TM</sup> control valve. The dome-loading regulator is used for a large drop in pressure from the air tanks and maintains an output pressure of 1.4 MPa. The Fisher control valve is used for the fine control of the tunnel stagnation pressure and is operated from a PC-based LabVIEW data acquisition program. Two inline heaters with a total power of 300 kW, capable of heating the air to 700 K, are installed to raise the stagnation temperature of the incoming air and prevent condensation in the test section. The test section Mach number can be varied using interchangeable nozzle blocks. Current experiments were performed at a test section Mach number of 1.5. The run time of the tunnel at these conditions is 90 seconds. The test section is 305 mm long, 102 mm wide, and 76 mm high, and has optical access from the sides and bottom. The SJA array is mounted on the tunnel ceiling. The stagnation pressure and temperature are typically maintained at 138 kPa and 316 K, respectively. A LabVIEW-based data acquisition program is used to control the wind tunnel and to measure and record the run conditions.

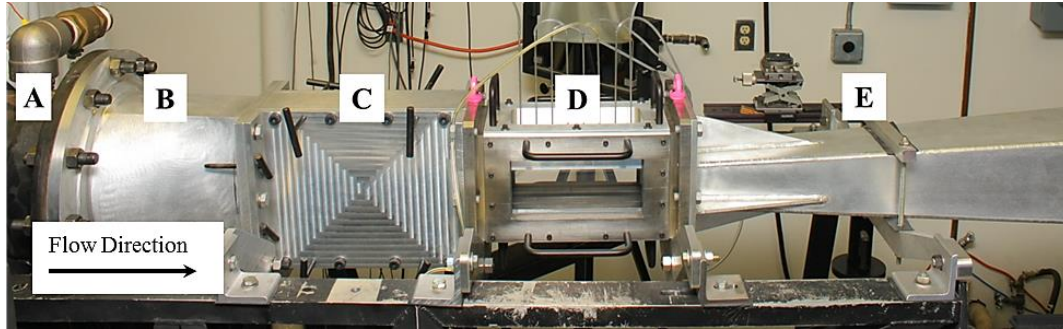


**Figure 4.1:** Layout of the supersonic wind tunnel; a) settling chamber; b) transition from circular to rectangular geometry; c) changeable nozzle block liners; d) test section; e) diffuser.

#### 4.1.1. Tunnel Flow Visualizations

A Z-type focusing shadowgraph system with two parabolic and two  $45^\circ$  mirrors was used for wind tunnel flow visualization. The light source used was a white-light Xenon flash lamp capable of being pulsed up to a frequency of 1 kHz with a pulse duration of  $5\ \mu\text{s}$ . While the SparkJet was operating in single-shot mode, a LaVision Imager Pro-X camera was used with DaVis software for image acquisition. The SparkJet, light source, camera, and data acquisition were triggered using a DG-535 delay generator as shown in Figure 4.2.

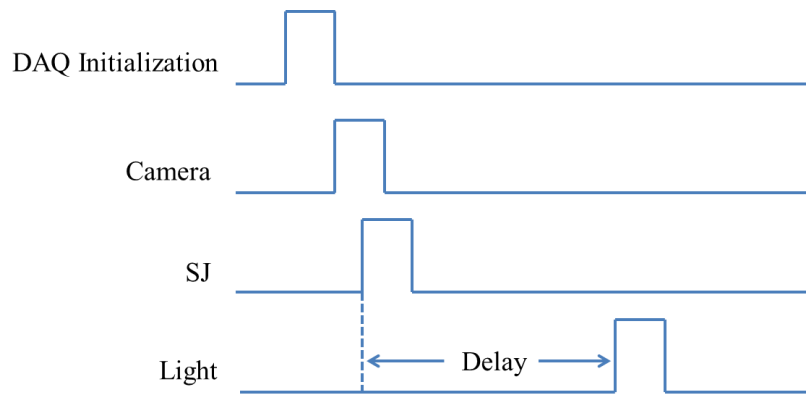


**Figure 4.2:** Phase-conditioned timing diagram for wind tunnel SJA tests.

An IDT model Y5 high speed camera controlled by Motion Studio was used to acquire images during burst mode operation of the SparkJet. The additional hardware required for acquiring images and data in burst mode is presented in Figure 4.3 and contained in the

black dashed lines. Two DG-535 delay generators were used to trigger the data acquisition, light source, camera, and a Laser Lock Model 88 Strobe Synchronizer frequency divider, at a frequency of 700 Hz. A 1 Hz signal output from the frequency divider was used to trigger an Agilent function generator, which output a 40 pulse burst at 700 Hz to trigger the SparkJet actuator. The system is used to send high-frequency bursts to the SparkJet to limit the possibility of thermal runaway previously mentioned. Trigger signals from the function generator and the light source were acquired to monitor jitter in the system which was measured as  $\pm 1 \mu\text{s}$ .

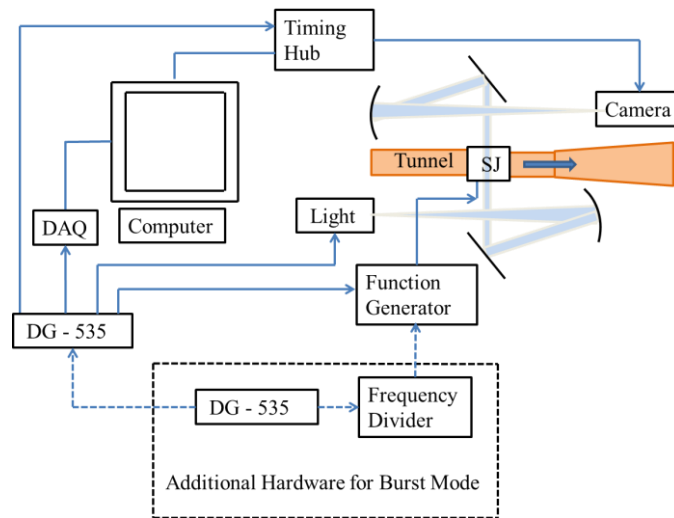


**Figure 4.3:** Wind tunnel testing hardware schematic.

Shadowgraph images of the SJA array installed and operating in the wind tunnel without tunnel flow were acquired to confirm reliable operation of the device and to visualize the actuator flow in the single-shot and burst operating modes. These quiescent flow tests were followed by supersonic flow tests beginning with baseline shadowgraph images for an inactive SparkJet array. Finally, phase-conditioned shadowgraph images of the SparkJet array operating in the single-shot and burst modes in a Mach 1.5 crossflow were acquired. Due to the intense EMI present while operating the SparkJet, the pressure sensor data obtained in close proximity to the actuator was contaminated and was therefore not used.

#### 4.2. Actuators under Quiescent Ambient Conditions

The shadowgraph images shown in Figure 4.4 are of the SparkJet operating in single-shot mode with no flow in the tunnel. The entire 76 mm height (h) of the test section is visualized in these images. Since the shadowgraph technique provides an integrated image over the entire optical path of the light these images show the SparkJet array such that the flowfield from all twelve jets are superimposed on each other (the array location is marked by the white dashed lines in all images).

Multiple blast waves, as well as the jet exhaust, can be seen in all of the images. The image at a time delay of 100  $\mu\text{s}$  reveals that the jet front has propagated roughly 5 mm away from the actuator while the extent of the furthest blast wave is roughly at the center of the test section (38 mm). The average velocity of the blast wave and jet front, measured from the initial discharge to 100  $\mu\text{s}$  after the initial discharge, are 430 m/s and 87 m/s, respectively. These values correlate well with the velocities found during the benchtop testing of the actuators. Comparisons between the benchtop velocity measurements and quiescent wind tunnel velocity measurements reveal that the jet front loses momentum more quickly than the blast wave. The trend observed in benchtop studies where the blast waves propagate at a much greater velocity than the jet front continues to be observed in these images, and the blast waves can be seen to have traveled completely across the test section at a time delay of 200  $\mu\text{s}$ . The image corresponding to a time delay of 300  $\mu\text{s}$  shows the blast waves actually reflecting from the test section floor and traveling back towards the ceiling where the actuator is mounted. The reflected blast waves have reached the top of the test section by  $\sim 400 \mu\text{s}$ .

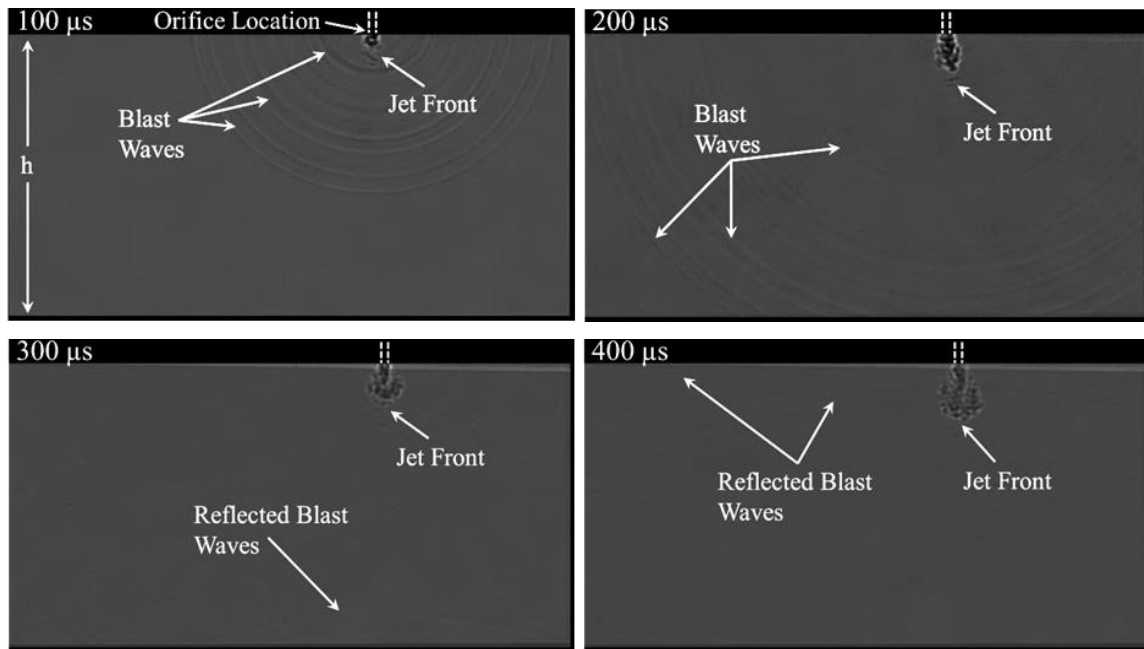


**Figure 4.4:** Shadowgraph images of the SJA array installed in the wind tunnel operating in single-shot mode with no freestream flow. (h = height of test section)

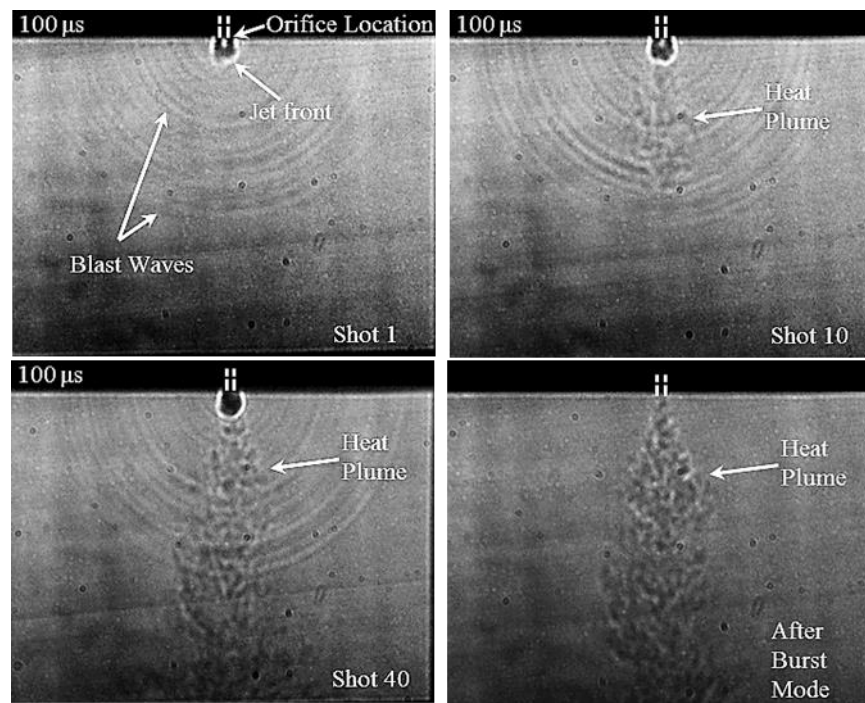


**Figure 4.5:** Instantaneous shadowgraph images of the SparkJet array installed in the wind tunnel operating in burst mode with no freestream flow in the test section.

The shadowgraph images shown in Figure 4.5 correspond to quiescent flow tests in burst mode with the SparkJet being discharged 40 times at a rate of 700 Hz. The first image in Figure 4.5 shows the first discharge in the burst mode at a time delay of 100  $\mu$ s and reveals essentially the same flow features of a jet front and multiple blast waves as the corresponding single-shot mode image in Figure 4.4. However, as the SparkJet array continues to discharge in burst mode, a noticeable thermal heat plume appears and propagates away from the SparkJet array orifices as seen in the following images at time delays of 100  $\mu$ s. The last image shows that the heat plume continues to be visible after the SparkJet has stopped discharging as evident by the lack of blast waves and presence of a heat plume. These results suggest that the accumulation of thermal energy in burst mode may have an appreciable impact on the actuator throughput, especially if the burst mode involves a large number of pulses.

### 4.3. Baseline Results (No Actuation)

A shadowgraph image of the freestream flow was acquired prior to actuator operation and is shown in Figure 4.6. The flow direction is from left to right and the field of view spans the entire test section height. The Mach waves seen in the image are oriented at approximately  $43^\circ$  (corresponding to  $M_\infty \sim 1.47$ ). The first Mach wave is due to a surface joint between the nozzle block and the test section, and the second is due to the array of SJA orifices. In results presented subsequently, the oblique shocks generated by the SparkJet flow can be compared to the baseline image and allows for an estimate to be made of the flow turning angle due to SJA operation.

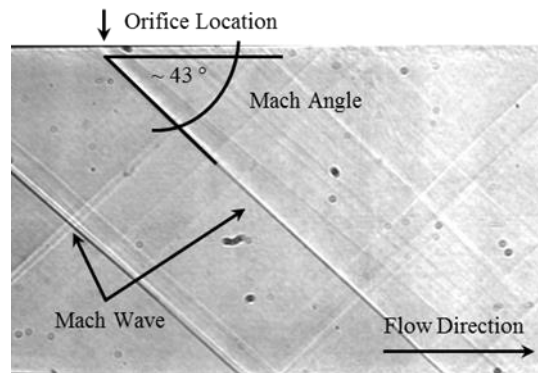


**Figure 4.6:** Baseline, no actuator flow, shadowgraph image of the test section.

#### **4.4. SJA in Single-Shot Mode in Supersonic Crossflow**

The SparkJet actuator was subsequently operated in single-shot mode in the Mach 1.5 crossflow. As before, the shadowgraph images shown in Figure 4.7 were taken at progressively increasing time delays between the light source trigger and the SparkJet discharge. In addition to the Mach wave due to the surface joint, these images clearly reveal a stronger oblique shock originating at the SparkJet array and followed by an expansion fan. These features have been marked in Figure 4.7 for clarity. The time-resolved images reveal that the oblique shock develops progressively and propagates across the test section with increasing time delays. The images corresponding to delays of 75 through 275  $\mu\text{s}$  reveal the presence of blast waves downstream of the oblique shock in the expansion fan where these blast waves propagate away from the SparkJet orifices. The propagating blast waves interact with the oblique shock wave where this interaction appears as a slight ‘kink’ in the oblique shock which moves concomitantly with the blast waves.

Comparisons between the images in Figure 4.4, taken with quiescent flow conditions, and those shown here reveal that the blast waves created by the actuator may possibly have a stronger effect on the flowfield than the jets issuing from the SJA. The oblique shock generated by the actuator follows the blast waves and propagates across the test section at a greater rate than the jet front. The jet flow is nevertheless critical as it acts as a jet in supersonic crossflow, producing and sustaining the oblique shock.

The momentum throughput from the SJA also determines the maximum oblique shock angle. The oblique shock angle evolution as a function of time is plotted in Figure 4.8. The image corresponding to a time delay of 350  $\mu\text{s}$  shows that the oblique shock has propagated across the entire height of the test section and has a measured angle of  $47^\circ$ . The oblique shock angle is approximately  $46^\circ$  at a time delay of 500  $\mu\text{s}$ , and it is at an angle of  $45^\circ$  at a delay of 700  $\mu\text{s}$  after the SparkJet has discharged. It is reasonable to assume that the shock wave will asymptotically return to a Mach wave at extended time delays. An important property of this study is to determine the upper limit of the effect of the SJA generated flow. As seen here, under the present conditions, a maximum oblique

shock angle of approximately  $48^\circ$  occurs 250 to 275  $\mu\text{s}$  after the SparkJet is discharged. This is equivalent to a  $5^\circ$  flow turning angle, a significant impact on this supersonic flow. The actuator/flow response is also noteworthy for the rapid rate at which this occurs – where the flow begins to measurably respond in  $\sim 50$   $\mu\text{s}$  or less, making SJAs potentially useful for supersonic flows. The very rapid flow response becomes more evident in the results discussed next.

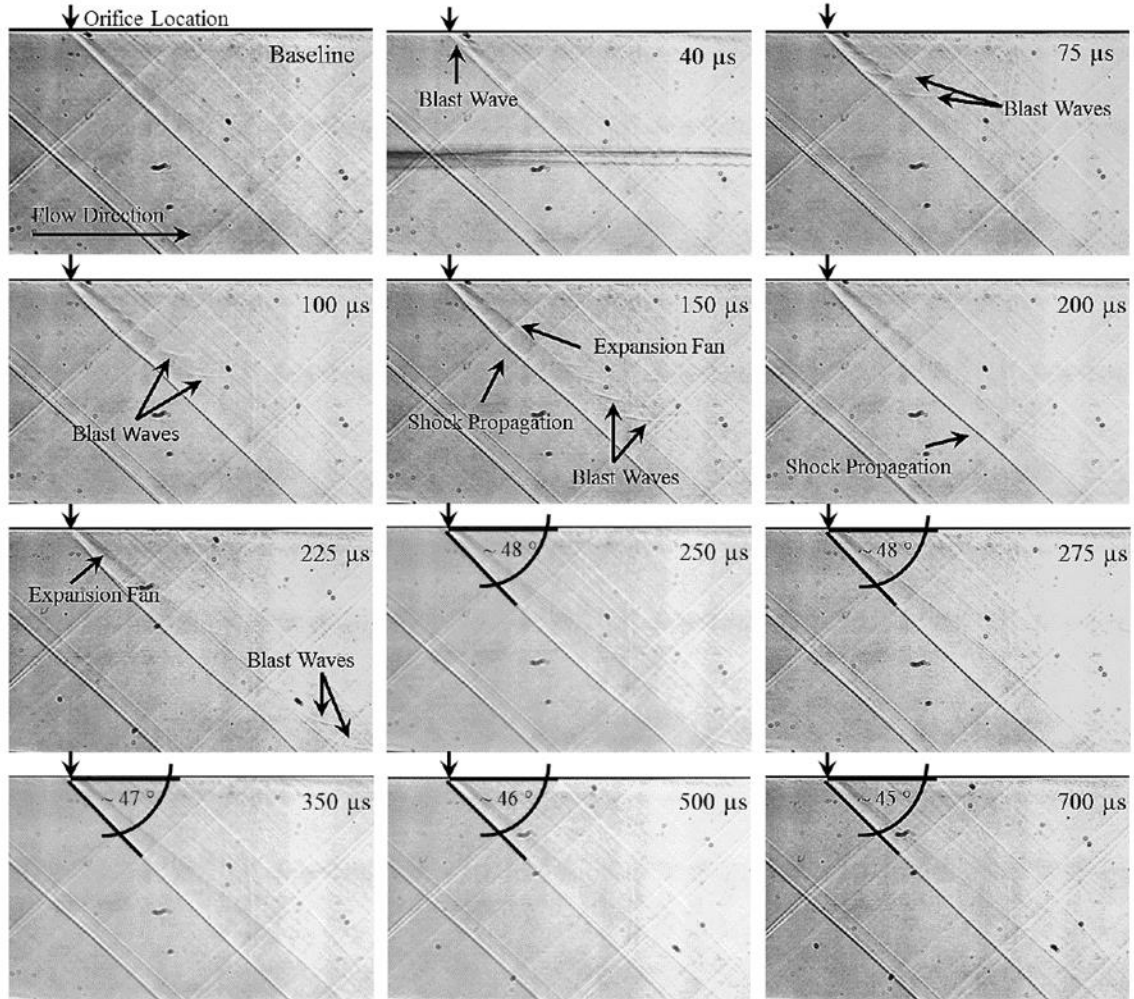


**Figure 4.7:** Phase-conditioned shadowgraph images of the SJA array (single-shot mode) in Mach 1.5 flow at various time delays.



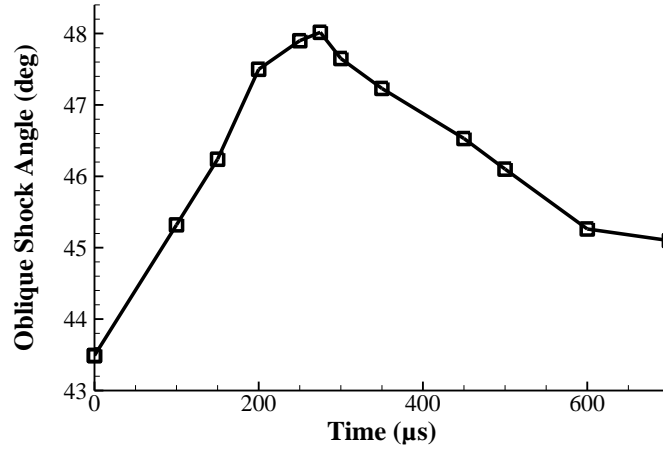


**Figure 4.8:** Oblique shock angle evolution.

Shadowgraph images were also obtained over a smaller field of view to visualize the flowfield in greater detail; shorter time delays were used in order to examine the early evolution of the flow from 0 to 100  $\mu\text{s}$ . The resulting images can be seen in Figure 4.9. The blast waves created by the SparkJet are first seen at a time delay of 20  $\mu\text{s}$  when they are observed to propagate away from the wall with increasing time delays. The oblique shock that is generated follows the blast waves and has nearly propagated across the entire field of view by 100  $\mu\text{s}$ . The shadowgraph images shown in Figures 4.7 and 4.9 confirm the SparkJet actuator's control authority in the supersonic flow and allow for a direct comparison to be made between the influence of the pulsed SparkJet actuator to the previously studied influence of steady microjet injection in supersonic crossflow (Kumar et al. 2011). This comparison is made in §4.6.

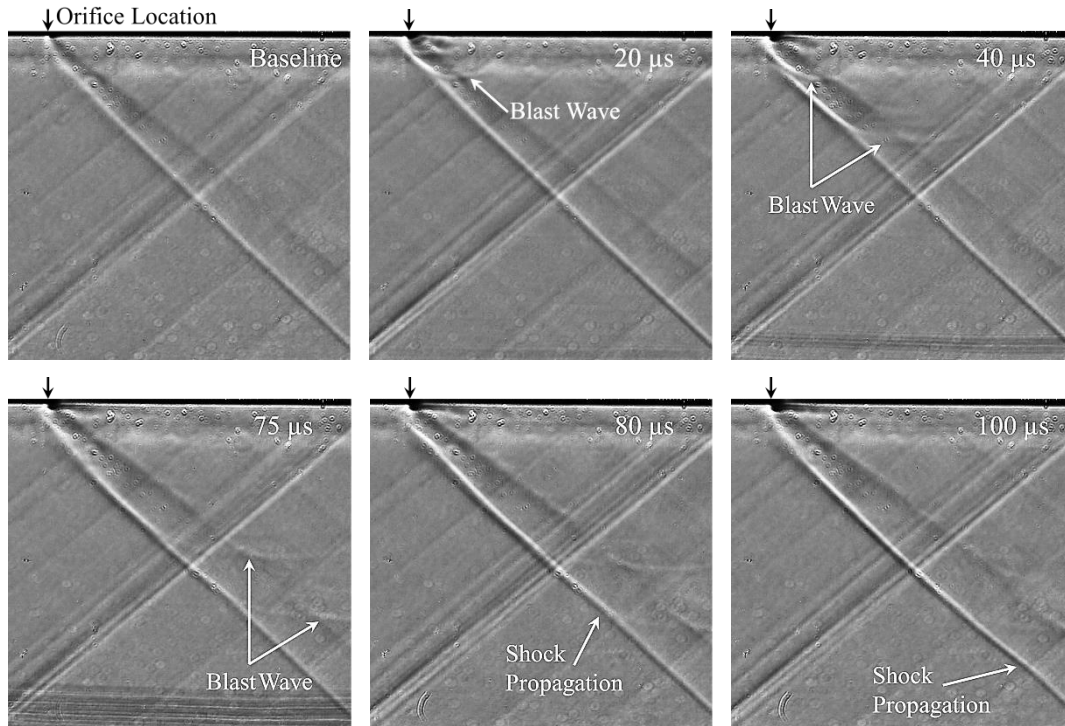


**Figure 4.9:** Phase-conditioned shadowgraph images showing boundary layer interaction in Mach 1.5 flow.

#### 4.5. SJA in Burst Mode in Supersonic Crossflow

The SJA was operated in burst mode and discharged 40 times at a frequency of 700 Hz to study and compare its effectiveness to the single-shot operating mode. Instantaneous shadowgraph images of the 40<sup>th</sup> discharge in burst mode are shown in Figure 4.10. The burst mode operation of the actuator creates flow features similar to those seen in the single shot operating mode. Blast waves can be seen in the images corresponding to 100, 200, and 250  $\mu\text{s}$  time delays. The blast waves are followed by an oblique shock that propagates across the test section with increasing time delays. The angle of SJA-generated oblique shocks reveal that at a time delay of 200  $\mu\text{s}$ , the 40<sup>th</sup> discharge of the actuator generates a  $47.2^\circ$  oblique shock. This oblique shock angle is the same as that generated by the 1<sup>st</sup> discharge in burst mode at the same time delay. Hence this later, improved version of the SJA is more reliable in burst mode than the SJA tested in benchtop studies discussed in chapter 3.

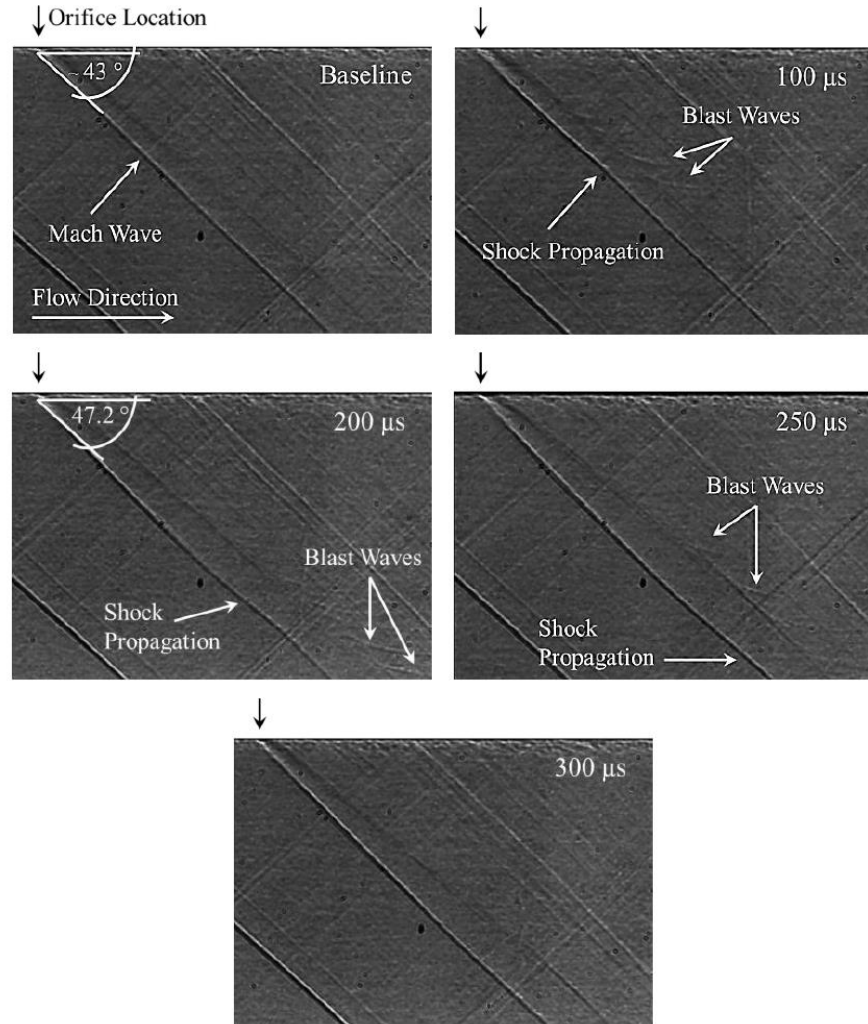


**Figure 4.10:** Phase-conditioned shadowgraph images of SJA operating at 700 Hz in burst mode.

A plot of the oblique shock angle evolution created by the first and last discharges in the operating sequence can be seen in Figure 4.11. The graph shows that the strength of the oblique shock angle created by the last discharge of the operating sequence is similar to the first in the sequence. It follows that the momentum throughput from the 1<sup>st</sup> discharge is almost identical to the 40<sup>th</sup> discharge indicating that the refresh cycle is completed by the time a subsequent discharge occurs. The matching oblique shock angles at a time delay of 200  $\mu$ s reveal that there is no apparent relation between the SparkJet discharge frequency of 700 Hz and the external flow.

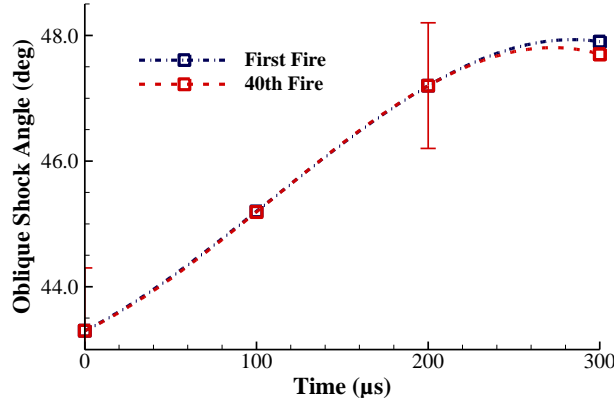


**Figure 4.11:** Oblique shock angle evolution comparing first and last discharge of the actuator operating in burst mode at 700 Hz.

#### 4.6. Comparison to Steady Microjets

Here, we compare the effect of the SparkJet array to the previously reported work involving steady microjets in the same wind tunnel facility under similar conditions. A plot of the oblique shock angle created by steady microjets at various microjet pressure ratios (MPR) and also of the oblique shock angle created by the SparkJet is shown in Figure 4.12. MPR is defined as the ratio of microjet supply pressure to the tunnel stagnation pressure. Arrays A2 and A3 were at different streamwise locations and, therefore, the boundary layer conditions were slightly different for each array. This plot shows that the microjet array performance was not affected by the change in boundary layer conditions and, in fact, the effect of the microjet versus MPR is nearly linear.

To compare the effect of the steady microjets with the unsteady SparkJet array, the maximum oblique shock angle of  $48^\circ$  is represented by the red dashed line and the intersection of this line with the linear approximation of the steady microjet performance is shown by the filled red circle. This comparison suggests that the maximum influence from the tested SparkJet array is nearly as effective as the steady microjets at an MPR of 3.2.

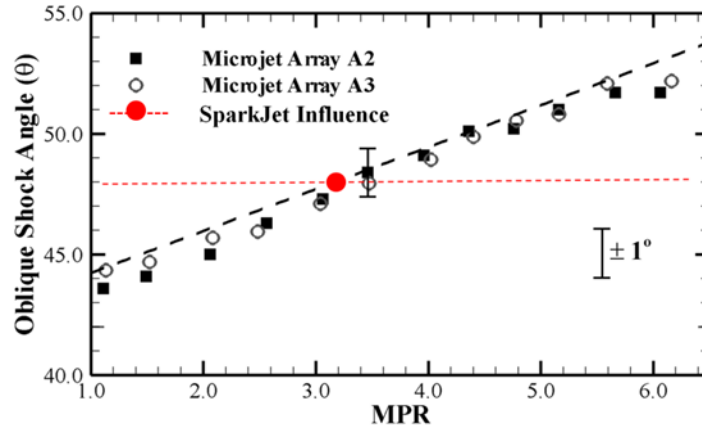


**Figure 4.12:** Oblique shock angle resulting from steady microjet injection and from the SparkJet actuator.

#### 4.7. REM Actuator – Selected Results

For comparison with the SparkJet actuator and steady microjet injection from previous studies, a REM actuator was designed with an operating frequency of nearly 1 kHz for use in wind tunnel experiments. The primary geometric features of this actuator are similar to those of the SJA, i.e. the microjet diameter, jet-jet spacing, number of jets, and jet injection location. Characterization of this actuator inside of the supersonic tunnel revealed a clear and sustainable response near 800 Hz. Phase-conditioned images were obtained using the Z-type shadowgraph system described in §4.1.1. For these visualizations, the jets are oriented in the primary optical axis direction, as with the SJA, leading to the images having an integrated view of the actuator flowfield. Figure 4.13 shows a sample of the phase-conditioned images that were obtained in quiescent ambient conditions in the tunnel. Here, the strong actuation results in visible shock cells in the actuator flowfield and acoustic waves that are visible inside the tunnel test section. Since this is an integrated visualization and the pulsed microjets have some phase jitter, there is some ‘smearing’ of certain flow features. The representative images shown here provide valuable insight into the jets’ development and structure.

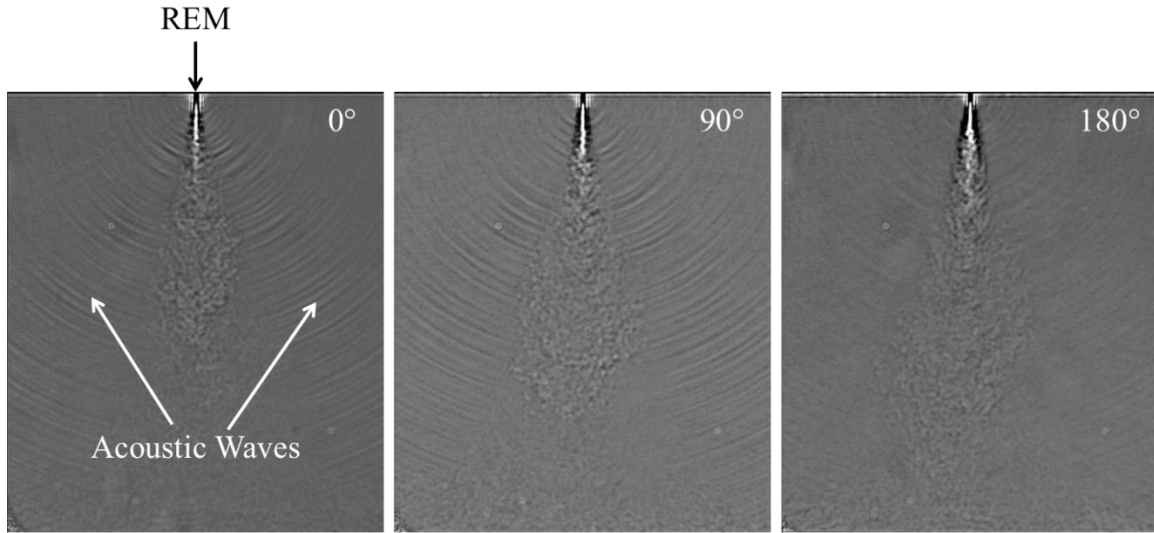


**Figure 4.13:** Phase-conditioned images of a  $\sim 1$  kHz REM actuator inside the supersonic tunnel without flow.

Baseline visualizations were acquired by running the tunnel at Mach 1.5 with no actuator flow. A baseline shadowgraph image is shown in Figure 4.14a. The location of the REM actuator and an unsteady pressure transducer located downstream of the actuator are indicated. A Mach wave with an angle of  $43^\circ$  is generated at the intersection of the actuator and the remainder of the test section block, as with the SJA. Phase-conditioned images with the actuator operating are seen in Figures 4.14b-d. From these visualizations, it can be seen that the unsteady actuation produces an oblique shock in the supersonic crossflow. The maximum oblique shock angle for the REM actuator is measured at  $50.7^\circ$  as seen in Figure 4.14c. A summary of the oblique shock angles obtained throughout the actuator cycle are shown in Figure 4.15.

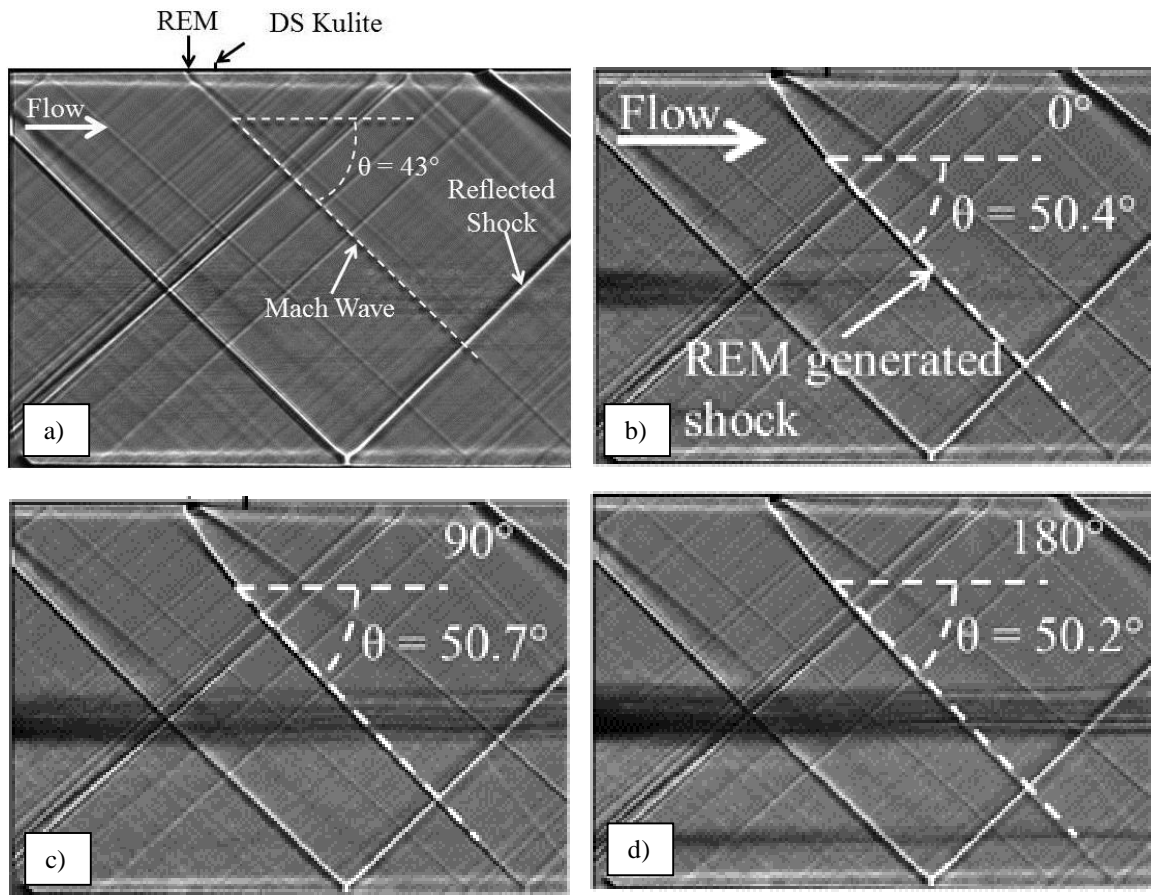


**Figure 4.14:** Shadowgraph images of REM actuation into Mach 1.5 crossflow. a) Baseline flow (no actuation); b) actuator on,  $0^\circ$  phase; c)  $90^\circ$  phase; d)  $180^\circ$  phase.

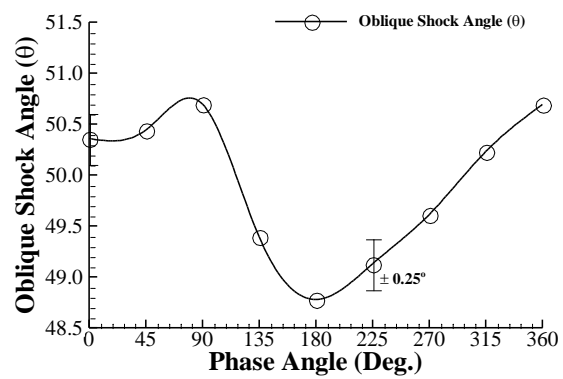


**Figure 4.15:** Angle of the actuator-generated oblique shock throughout the actuator cycle.

Earlier studies using steady microjet injection in a supersonic crossflow (Kumar et al. 2011) have shown a correlation between the microjet supply pressure ratio, MPR, and the generated oblique shock angle (Ali et al. 2010). A comparison to these results can be seen in Figure 4.16. For the same pressure ratio, the unsteady actuation from the REM actuator produces a range of oblique shock angles that is slightly lower than the shock angle produced by steady actuation. Although unsteady actuation is unable to generate the same oblique shock angles as steady microjet injection, the ability to produce an oblique shock whose angle varies at a controllable frequency is a unique feature of the REM actuators.

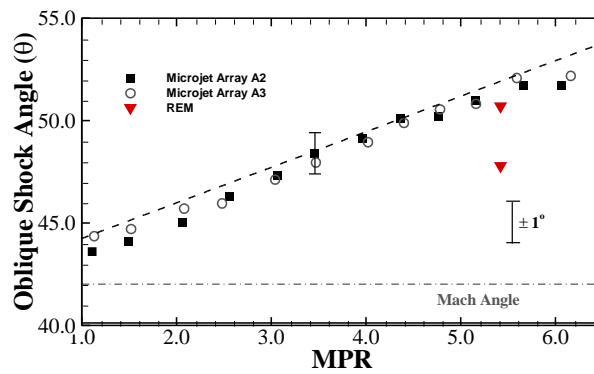


**Figure 4.16:** Comparison of REM actuator performance to steady microjet injection (Ali et al. 2010).



## 5. Summary and Conclusions

Driven by the need to effectively control high-speed flows using Active Flow Control (AFC) schemes, a plasma-based actuator, the SparkJet Actuator (SJA), was the focus of this multi-year study sponsored by the Air Force Office of Scientific Research (AFOSR). In a collaborative effort with JHU/APL, the performance of the SJA was carefully characterized over a wide parametric space where the lessons learned led to design improvements in subsequent generations of actuators. Finally, the actuator was tested under supersonic conditions to characterize and understand the actuator and flow behavior in a canonical high speed flow.

In this report, we mainly summarized the results of the study conducted at the Florida State University's Florida Center for Advanced Aero-Propulsion (FSU-FCAAP) that focused on experimentally characterizing the properties of the unsteady flow produced by the SparkJet actuator. The FSU portion of this investigation relies heavily on high-resolution, time-resolved flow visualization methods, including some highly specialized ones, such as Laser Based Micro-Schlieren (LBMS). These methods are applied to better understand the dynamics of the flow emanating from the SJA under quiescent and supersonic ambient conditions. The development, modeling, and fabrication of the SJA was the responsibility of our collaborators at JHU/APL. The details of the actuator design, modeling, and the dependence of actuator performance on factors such as material choices, electrode design, etc., are described in a companion report by the JHU/APL team.

A number of SJA variants were first carefully characterized in benchtop studies. Based on these results and in close collaboration with the FSU partners, JHU/APL implemented improvements in subsequent generations of SJAs. The main outcome of the benchtop studies using LBMS were as follows:

- The SJAs have a *very rapid response* producing blast waves and high momentum jets fronts in less than  $10\mu\text{s}$ . This is very attractive for high-speed flow control, especially for closed loop control, if some of the reliability and EMI issues can be addressed.

- The maximum velocity of the blast waves at atmospheric conditions was found to be around 410 m/s while the maximum jet front velocity was found to be 310 m/s.
- At sub-atmospheric quiescent ambient conditions, the jet front propagation velocity is significantly higher, suggesting possibly higher control authority for high-altitude AFC applications.
- Burst mode operation of the SJA was examined at frequencies up to 1 kHz. While the later generation of SJA produced flows similar to single shot mode, the reliability dropped significantly after 40-50 consecutive shots. It is suspected that this is in part due to thermal management issues when operating at high repetition rates. This is a problem that must be examined and addressed in future work.
- Overall, the two electrode design that uses a ‘pseudo-series trigger’ mechanism was found to lead to better reliability and performance of the SJA and was used in the later generation of SJAs. (This led to more than doubling of the SJA operating efficiency; see JHU/APL report for details)

Benchtop studies were followed by SJA implementation and testing in a Mach 1.5 crossflow where the flow response was characterized using a time-resolved/phase-conditioned shadowgraph method. Supersonic flow studies revealed that:

- SJAs have excellent control authority in supersonic flow as seen by the unsteady jets and blast waves issuing from the SJA.
- The SJA flow dynamically generated reasonably strong shocks and did so very rapidly. Based on the results, the supersonic flow begins to measurably respond to actuation *in less than 50 $\mu$ s*.
- For the actuators examined here, the SJAs were able to very rapidly generate oblique shocks corresponding to a maximum turning angle  $\sim 5^\circ$ .
- SJA were also operated in burst mode at 700 Hz. Their performance was found to be reliable and highly repeatable for up to 40-50 shots.

Some of the potential problems encountered include very high EMI, which precludes (or makes very challenging) most traditional sensor based measurements. The ability to

operate at high repetition rates for longer bursts will also make the SJAs significantly more attractive for a wider range of high-speed applications.

In summary, through this collaborative approach, we were able to systematically study, understand, and improve the design, operation, and reliability of SparkJet actuators. The extremely fast response time, the very high control authority – clearly demonstrated in this study, combined with its compact size and ZNMF property makes SJA an option worth exploring, especially for supersonic and hypersonic flows. However, the reliability of SJA still needs improvement. Improvement that is more likely through similar collaborative research such as the present study that leverages the expertise of its partners.

## 6. References

1. Alvi, F.S., Shih, C., Elavarasan, R., Garg, G. and Krothapalli, A., "Control of Supersonic Impinging Jet Flows Using Supersonic Microjets," *AIAA Journal*, Vol. 41, No. 7, 2003, pp. 1347-1355.
2. Brocher, E., Maresca, C. and Bournay, M. H., "Fluid Dynamics of the Resonance Tube," *Journal of Fluid Mechanics*, Vol. 43, Part 2, 1970, pp 369-384.
3. Bryant, R. G., Fox, R. L., Lachowicz, J. T. and Cheri, F.J., "Piezoelectric Synthetic Jets for Aircraft Control Surfaces," *SPIE Paper 3674*, 1999.
4. Caraballo, E., Webb, N., Little, J., Kim, J.-H. and Samimy, M., "Supersonic Inlet Flow Control Using Plasma Actuators," *AIAA Paper 0924*, 2009.
5. Cattafesta, L., Mathew, J., Wang, W. and Kurdila. A., "Modeling of Piezoelectric Actuators for Fluid Flow Control," *SAE Paper 01-5534*, 2000.
6. Corke, T. C., Enloe, C. L. and Wilkinson, S. P., "Dielectric Barrier Discharge Plasma Actuators for Flow Control," *Annual Review of Fluid Mechanics*, Vol. 42, 2010, pp 505-529.
7. Cutler, A. and Drummon, J. P., "Toward a High-Frequency Pulsed-Detonation Actuator," *AIAA paper 555*, 2006.
8. Cybyk, B. Z., Grossman, K. R. and Wilerson, J. T., "Single Pulse Performance of the SparkJet Flow Control Actuator," *AIAA Paper 401*, 2005.
9. Cybyk, B. Z., Simon, D. H. and Land, H. B., III, "Experimental Characterization of a Supersonic Flow Control Actuator," *AIAA Paper 478*, 2006.
10. Dziuba, M. and Rossmann, T., "Active control of a Sonic Transverse Jet in a Supersonic Cross Flow using a powered Resonance tube," *AIAA Paper 897*, 2005.
11. Emerick, T. M., "Sparkjet Development and Characterization for High Speed Flow Control," *MS thesis*, Florida State University, 2013.
12. Foster, C. H., "Characterizing High Frequency Microscale Flows Using Optical Methods," *MS thesis*, Florida State University, 2011.
13. Ganiev, Y. C., Gordeev, V. P., Krasilnikov, A. V., Lagutin, V. I., Otmennikov, V. N. and Panasenکو, A. V., "Theoretical and Experimental Study of The Possibility of Reducing Aerodynamic Drag by Employing Plasma Injection," *AIAA Paper 1999-0603*.
14. Grossman, K. R., Cybyk, B. Z. and Van Wie, D. M., "Spark Jet Actuators for Flow Control," *AIAA Paper 57*, 2003.
15. Haack, S. J., Taylor, T. M., Cybyk, B. Z., Foster, C. H. and Alvi, F. S., "Experimental Estimation of SparkJet Efficiency," *AIAA Paper 3997*, 2011.
16. Haack, S. J., Taylor, T., Emhoff, J. and Cybyk, B., "Development of an Analytical SparkJet Model," *AIAA Paper 4979*, 2010.

17. Hartmann, J. and Trolle, B., "A new acoustic generator," *Journal of Scientific Instruments*, Vol. 4, No. 4, 1927, pp 101-111.
18. Jacob, J. D., Rivir, R., Carter, C. and Estevadeordal, J., "Boundary Layer Flow Control using AC Discharge Plasma Actuators," *AIAA Paper 2128*, 2004.
19. Joslin, R. D., Horta, L. G. and Chen, F.J., "Transitioning Active Flow Control to Applications," *AIAA Paper 3575*, 1999.
20. Kalra, C. S., Zaidi, S. H., Shneider, M. N. and Miles, R. B., "Shockwave Induced Turbulent Boundary Layer Separation Control with Plasma Actuators," *AIAA Paper 1002*, 2009.
21. Kalra, C., Zaidi, S., Alderman, B., Miles, R. and Murt, Y., "Magnetically Driven Surface Discharges for Shock-Wave Induced Boundary-Layer Separation Control," *AIAA Paper 222*, 2007.
22. Kastner, J. and Samimy, M., "Development and Characterization of Hartmann tube fluidic actuators for high-speed flow control," *AIAA Journal*, Vol. 40, No.10, 2002, pp. 1926-1934.
23. Kelley, C., Bowles, P., Cooney, J., He, C. and Corke, T., "High Mach number Leading-Edge Flow Separation Control Using AC DBD Plasma Actuators," *AIAA Paper 0906*, 2012.
24. Kumar, R., Ali, M. Y., Alvi, F. S. and Venkatakrishnan, L., "Generation and Control of Oblique Shocks Using Microjets," *AIAA Journal*, Vol. 49, No. 12, 2011.
25. Kumar, R., Lazic, S. and Alvi, F. S., "Control of High Temperature Supersonic Impinging Jets Using Microjets," *AIAA Journal*, 2009, Vol. 47, No. 12, pp. 2800-2811.
26. List, J., Byerley, A., McLaughlin, T. and Dyken, R. V., "Using a Plasma Actuator to Control Laminar Separation on a Linear Cascade Turbine Blade," *AIAA Paper 1026*, 2003.
27. McManus, K., and Magill, J., "Separation Control in Incompressible and Compressible Flows using Pulsed Jets," *AIAA Paper 1948*, 1996.
28. Phalnikar, K. A., Kumar, R. and Alvi, F. S., "Experiments on Free and Impinging Supersonic Microjets," *Experiments in Fluids*, Vol. 44, 2007.
29. Raman, G. and Kibens, V., "Active Flow Control using Integrated Powered Resonance tube Actuators," *AIAA Paper 3024*, 2001.
30. Samimy, M., Adamovich, I., Webb, B., Kastner, J., Hileman, J., Keshav, S. and Palm, P., "Development and characterization of plasma actuators for high-speed jet control," *Experiments in Fluids*, Vol. 37, 2004.
31. Samimy, M., Kearney-Fisher, M., Kim, J. and Sinha, A., "High speed and High Reynolds Number Jet Control Using Arc Filament Plasma Actuators for Noise Mitigation and for Flow and Noise Diagnostics," *AIAA paper 2011-22*.

32. Samimy, M., Kim, J.-H., Kastner, J., Adamovich, I. and Utkin, Y., "Active control of high-speed and high-Reynolds-number jets using plasma actuators," *Journal of Fluid Mechanics*, Vol. 578, 2007.
33. Scroggs, S. D. and Settles, G. S., "An Experimental Study of Supersonic Microjets," *Experiments in Fluids*, Vol. 21, 1996.
34. Seifert, A., Darabi, A. and Wygnanski, I., "Delay of Airfoil Stall by Periodic Excitation," *Journal of Aircraft*, Vol. 33, No. 4, 1996, pp. 691-698.
35. Settles, G., *Schlieren and Shadowgraph Techniques: Visualizing Phenomena in Transparent Media*. Springer-Verlag Berlin Heidelberg, 2<sup>nd</sup> Edition, 2006.
36. Shang, J. S., Kimmel, R. L., Menart, J. and Surzhikov, S.T., "Hypersonic Flow Control Using Surface Plasma Actuator," *Journal of Propulsion and Power*, Vol. 24, No. 5, 2008.
37. Smith, B. L., and Glezer, A., "The Formation and Evolution of Synthetic Jets," *Physics of Fluids*, Vol. 10, No. 9, 1998, pp. 2281-2297.
38. Solomon, J. T., "High-Bandwidth Unsteady Micro-Actuators for Active Control of High-Speed Flows," *PhD dissertation*, Florida State University, 2010.
39. Stanek, M. J., Raman, G., Kibens, V., Ross, J. A., Odedra, J. and Peto, J. W., "Control of Cavity Resonance Through Very High Frequency Forcing," *AIAA Paper 1905*, 2000.
40. Volpe, J. and Settles, G., "Laser-induced Gas Breakdown as a Light Source for Schlieren and Shadowgraph Particle Image Velocimetry," *Optical Engineering*, Vol. 45, 2006.
41. Webb, N., Clifford, C. and Samimy, M., "An Investigation of the Control Mechanism of Plasma Actuators in a Shock Wave-Boundary Layer Interaction," *AIAA Paper 0402*, 2013.
42. Wiltse, J. M. and Glezer, A., "Direct Excitation of Small Scale Motions in Free Shear Flows," *Physics of Fluids*, Vol. 10, No. 8, 1998, pp 2026-2036.
43. Wiltse, J. M., and Glezer, A., "Manipulation of Free Shear Flows Using Piezoelectric Actuators," *Journal of Fluid Mechanics*, Vol. 249, 1993, pp. 261-285.
44. Yeung, P. K., Brasseur, J. G. and Wang, Q., "Dynamics of Direct Large-Scale Couplings in Coherently- Forced Turbulence: Concurrent Physical-Space and Fourier-Space Views," *Journal of Fluid Mechanics*, Vol. 283, 1995, pp 43-95.
45. Zhuang, N., Alvi, F.S., Alkislar, M.B. and Shih, C., "Supersonic Cavity Flows and their Control," *AIAA Journal*, Vol. 44, No. 9, 2006, pp. 2118-2128.

## **7. Supplemental Information**

### **7.1. Publications (2008 – 2013)**

#### **7.1.1. Archival Journal Publications Directly Related (Published, Under Review, and In Preparation)**

1. Popkin, S. H., Cybyk, B. Z., Foster, C. H. and Alvi, F. S., “Experimental Estimation of SparkJet Efficiency,” submitted to the AIAA Journal, , tentatively accepted after 2nd review with minor modifications. Anticipated publication: Summer 2014.
2. Emerick, T. Ali, M. Y., Alvi, F. S. and Popkin, S. H. “Characterization and Implementation of SparkJet Actuators in Supersonic Flow,” to be submitted to Experiments in Fluids, March/April 2014.
3. Uzun, A., Foster, C. H., Solomon J., Oates, W. S., Hussaini M. Y. and Alvi, F. S. “Flow Physics of a Pulsed Actuator Generating Unsteady Microjets,” AIAA Journal, Vol. 51, No. 12, Dec. 2013, pp. 2894-2918.
4. Ali, M. Y. Kumar, R., Alvi, F. S., Manisankar., C., Verma, S. B. and Venkatkrishnan, L., “Studies on the Control of Shock Wave-Boundary Layer Interaction Using Steady Microactuators,” AIAA Journal, , Vol. 51, No. 12, Dec. 2013, pp. 2753-2762.
5. Solomon, J., Foster, C. and Alvi, F. S. “Design and Characterization of High-bandwidth, Resonance Enhanced Pulsed Microactuators: A Parametric Study,” AIAA Journal, Vol. 51, No. 2, Feb. 2013.
6. Solomon, J., Foster, C. and Alvi, F. S. “Design and Characterization of High-bandwidth, Resonance Enhanced Pulsed Microactuators: A Parametric Study,” AIAA Journal, Vol. 51, No. 2, Feb. 2013.
7. Hogue, J. M., Kumar, R., Oates, W. and Alvi, F. S., “A Supersonic Broadband Microjet Actuator Using Piezohydraulic Actuation,” Journal of Intelligent Materials, Vol. 23 Issue 17, November 2012.
8. Kumar, V., Hays, M., Fernandez E., Oates, W. and Alvi, F. S., “Flow Sensory Actuators for Micro Air Vehicles,” Smart Mater. Structures, Vol. 20, September 2011.
9. Kumar, R., Ali, Y., Alvi, F. S. and Venkatkrishnan, L., “Generation and Control of Oblique Shocks Using Microjets,” AIAA Journal, 2011, Vol. 49, No. 12, pp. 2751-2759.
10. Alvi, F. S. and Cattafesta, L. N., “The Art and Science of Flow Control – Case Studies Using Visual and Optical Methods,” in “Revealing the Invisible- A Review of Flow Visualization Techniques,” European Physical Journal, Special Topics, Vol. 182, pp. 97–112 (2010).

### 7.1.2. Other Related Archival Journal Publications

1. Fernandez, E., Kumar, R. and Alvi, F. S., "Separation Control on a Low-Pressure Turbine Blade using Microjets," *Journal of Propulsion & Power*, Vol. 29, No. 4, 2013, pp. 867-881.
2. Kumar, R., Wiley, A., Alvi, F. S. and Venkatkrishnan, L. "Role of Coherent Structures in Supersonic Impinging Jets," *Physics of Fluids*, Vol. 25, 076101, July 2013.
3. Uzun, A., Kumar, R., Hussaini M. Y. and Alvi, F. S. "Simulation of Tonal Noise Generation by Supersonic Impinging Jets," *AIAA Journal* Vol. 51, No. 7, July 2013, pp 1593-1611.
4. Kumar, V. and Alvi, F. S., "Towards Understanding and Optimizing Separation Control Using Microjets," *AIAA Journal*, 2009, Vol. 47, No. 11, pp. 2544-2557.
5. Arunajatesan, S., Kannepali, C., Sinha, N., Sheehan, M., Alvi, F. S., Shumway, G. and Ukeiley, L., "Suppression of Cavity Loads Using Leading Edge Blowing," *AIAA Journal*, 2009.
6. Alvi, F. S., H. Lou, C., Shih, C and R. Kumar., "Experimental study of physical mechanisms in the control of supersonic impinging jets using microjets," *Journal of Fluid Mechanics*, Vol. 613, 2008, pp. 55-83, 2008.
7. Ahmed, K. Ali, M. Y. and Alvi, F. S., "Mixing Characteristics of Active Microjet-Based Actuators in a Supersonic Backward-Facing Step Flow," to appear in the *AIAA Journal*, (accepted for publication), expected publication date: Spring 2014.
8. Worden, T. J., Upadhyay, P., Gustavsson, J. P. and Alvi, F. S., "Studies on Microjet Control Effectiveness in High-Temperature Supersonic Impinging Jets," to appear in the *AIAA Journal*, (accepted for publication), expected publication date: Spring 2014.
9. Kreth, P. and Alvi, F. S., "Microjet-Based Active Flow Control on a Fixed Wing UAV," to appear in the *Journal of Flow Control, Measurement, and Visualization*, (accepted for publication), expected publication date: Spring 2014.

### 7.1.3. Conference Proceedings

1. Fernandez, E. and Alvi, F. S., "Vorticity Dynamics of Microjet Arrays for Active Control," AIAA Science and Technology Forum and Exposition, Maryland, Jan. 2014.
2. Ali, M. Y. and Alvi, F. S., "Three – dimensional Flowfield of Microjets in Supersonic Crossflow," 43rd AIAA Fluid Dynamics Conference and Exhibit, San Diego, June 2013.
3. Popkin, S. H. , Cybyk, B. Z., Land III, H. B., Emerick,, T., Ali, M., Foster C., Alvi, F., "Recent Performance-Based Advances in SparkJet Actuator Design for Supersonic Flow Applications," AIAA Paper 2013-0322, 51st, AIAA Aerospace Meeting and Exhibit, Grapevine TX, Jan. 2013.
4. Upadhyay, P., Gustavsson, J. and Alvi, F., "Ultra-High-Frequency Actuators for Jet Noise Control," AIAA Paper 2013-2476, 43rd AIAA Fluid Dynamics Conference and Exhibit, San Diego, June 2013.



5. Topolski, N., Arora, N., Ali, M.Y., Solomon, J.T. and Alvi, F.S., "Study on Resonance Enhanced Microactuators in Supersonic Crossflow", 42nd AIAA Fluid dynamics Conference and Exhibit 25-28 June 2012.
6. Garret, S., Solomon, J.T., Gustavson, G., Alvi, F.S., "Implementing Resonance Enhanced Microactuators for the control supersonic microjets", AIAA-0065, 2012.
7. Uzun, A., Foster, C.H., Solomon, J.T., Oates, W.S., Hussaini, M.Y., Alvi, F.S., "Simulations of Pulsed Microactuators of High -Speed Flow Control", AIAA-2938, 2011.
8. Kreth, P., Solomon, J.T., Alvi, F.S., "Resonance-Enhanced High Frequency Micro-actuators with Active Structures", AIAA-2939, 2011.
9. Foster, C., Solomon, J.T., Alvi, F.S., "Visual Study of Resonance dominated Microjet flows using laser based micro- Schlieren", AIAA-2011-766, 2011.
10. Ali, M.Y., Solomon, J.T., Gustavsson, J., Alvi, F.S., "Control of Supersonic Cavity Flows Using High Bandwidth Micro actuators", AIAA-197194-564, 2010.
11. Solomon, J.T., Alvi, F.S., Kumar, R., Gustavsson, J., "Principles of a High Bandwidth Micro-actuator Producing Supersonic Pulsed Microjets", AIAA-197237-476, 2010.
12. Solomon, J.T., Wiley, A., Kumar, R., Alvi, F.S., "Active and Adaptive Control of Supersonic flow using High Bandwidth Pulsed Micro-actuators", FCAAP meeting Aug 13-14 2009.
13. Solomon, J.T., Wiley, A., Kumar, R., Alvi, F.S., "Development and Implementation of High Frequency Pulsed Microactuators for Active Control of Supersonic Impinging Jet", SAROD meeting, National Aerospace Lab, India, 2009.
14. Solomon, J.T., Hong, S., Wiley, A., Kumar, R., Annswamy, A.M., Alvi, F.S., "Control of Supersonic Resonant flows Using High bandwidth Micro- Actuators", AIAA -3247, 2009.
15. Solomon, J.T., Kumar, R., Alvi, F.S., "Development and characterization of High bandwidth micro actuator", ASME FEDSM 55032, 2008.
16. Solomon, J.T., Kumar, R., Alvi, F.S., "High band width pulsed micro actuators for active flow control", AIAA-3042, 2008.

## **7.2. Students Supported under this Grant (Fully or Partially)**

1. Solomon, J.T., "High Bandwidth Pulsed Microactuators for Active Control of High Speed Flows," PhD dissertation, Florida State University, 2010.
2. Foster, C., M.S. Thesis, "Time-Resolved Studies of High-frequency Microscale Actuators," Summer 2011.
3. Thomas, E., M.S. Thesis, "Spark Jet Development and Characterization for High Speed Flow Control," Summer 2013

### **7.3. Honors and Awards (2009 – 2013)**

F.S. Alvi: Elected Fellow of American Society of Mechanical Engineers (ASME)

F.S. Alvi: Invited Professor at Université d'Orléans, France, 2009-2010

F.S. Alvi: FSU *Innovators Award*, 2006-08, 2010 & 2013

F.S. Alvi: *Engineering Research Award* – “In Recognition of Exceptional Achievement,” 2009

F.S. Alvi: Research & Entrepreneurship Award - College of Engineering, 2013

### **7.4. Related Patents (2009 – 2013)**

- Microjet Creation and Control of Shock Waves– Patent number 8,359,825 (2013)
- Microjet Control for Flow & Noise Reduction in Automotive Applications – Patent number 8303024 B. (2012)
- High Bandwidth & Control Authority Micro-Actuators for Active Flow & Noise Control (with R. Kumar & J. Solomon) – Patent number 8286895 B2 (2012)

### **Acknowledgement/Disclaimer**

This work is supported by the Air Force Office of Scientific Research, USAF, under AFOSR Grant number FA9550-09-1-0301. The views and conclusions contained herein are those of the authors and should not be interpreted as necessarily representing the official policies and endorsements, either expressed or implied, of the Air Force Office of Scientific Research or the U. S. Government.